AGU PUBLICATIONS

JGR

Journal of Geophysical Research: Atmospheres

RESEARCH ARTICLE
10.1002/2015JD023323

Key Points:
- Quelccaya snowfall linked to South American monsoon activity
- Most of Quelccaya snowfall is triggered by cold air incursions of midlatitude air
- Quelccaya seasonal δ^{18}O records summer precipitation and winter alteration at surface

Supporting Information:
- Figures S1–S4 and Sections S1 and S2

Correspondence to:
J. V. Hurley,
jvhurley12@gmail.com

Citation:
Hurley, J. V., M. Vuille, D. R. Hardy, S. J. Burns, and L. G. Thompson (2015), Cold air incursions, δ^{18}O variability, and monsoon dynamics associated with snow days at Quelccaya Ice Cap, Peru, *J. Geophys. Res. Atmos.*, *120*, doi:10.1002/2015JD023323.

Received 3 MAR 2015
Accepted 7 JUL 2015
Accepted article online 14 JUL 2015

Cold air incursions, δ^{18}O variability, and monsoon dynamics associated with snow days at Quelccaya Ice Cap, Peru

John V. Hurley[1], Mathias Vuille[1], Douglas R. Hardy[2], Stephen J. Burns[2], and Lonnie G. Thompson[3]

[1]Department of Atmospheric and Environmental Sciences, University at Albany, Albany, New York, USA, [2]Department of Geosciences, University of Massachusetts, Morrill Science Center, Amherst, Massachusetts, USA, [3]Byrd Polar Research Center, Ohio State University, Columbus, Ohio, USA

Abstract Quelccaya Ice Cap in the Andes of Peru contains an annually resolved δ^{18}O record covering the past 1800 years; yet atmospheric dynamics associated with snow deposition and δ^{18}O variability at this site are poorly understood. Here we make use of 10 years of snow pit and short core δ^{18}O data and hourly snow-height measurements obtained by an automated weather station deployed at the ice cap's summit to analyze linkages between snowfall, δ^{18}O, and the South American summer monsoon (SASM). Snow accumulation peaks in December and is negative May–September. Snow δ^{18}O values decrease gradually through austral summer from about −17 to −24‰. Surface snow δ^{18}O is altered after deposition during austral winter from about −24 to −15‰. More than 70% of the total snow accumulation is tied to convection along the leading edge of cold air incursions of midlatitude air advected equatorward from southern South America. Snowfall amplitude at Quelccaya Ice Cap varies systematically with regional precipitation, atmospheric dynamics, midtroposphere humidity, and water vapor δD. Strongest snowfall gains correspond with positive precipitation anomalies over the western Amazon Basin, increased humidity, and lowered water vapor δD values, consistent with the "amount effect." We discuss ventilation of the monsoon, modulated by midlatitude cold air advection, as potentially diagnostic of the relationship between SASM dynamics and Quelccaya snowfall. Results will serve as a basis for development of a comprehensive isotopic forward model to reconstruct past monsoon dynamics using the ice core δ^{18}O record.

1. Introduction

The ice core record collected from the diminishing Quelccaya Ice Cap (QIC; 70.82°W, 13.93°S; 5670 m above sea level) of Peru is the oldest and most precisely dated high-resolution paleoclimate record from the tropical Andes, covering the past millennium [*Thompson et al*., 1985]. Until recently, it was the only annually resolved record from the region. Over the past few years, however, additional highly resolved isotopic records from lake sediments and speleothems have become available [*Bird et al*., 2011; *Vuille et al*., 2012; *Kanner et al*., 2013; *Apaestegui et al*., 2014]. The ice δ^{18}O records from Quelccaya have traditionally been interpreted as proxies for temperature variability over the past ~1800 years. Yet others have questioned that interpretation and argued that the δ^{18}O in tropical ice cores is more likely responding to large-scale changes in atmospheric circulation and modes of climate variability such as El Niño–Southern Oscillation (ENSO) or changes in monsoon intensity upstream [*Bradley et al*., 2003; *Hoffman et al*., 2003; *Vuille et al*., 2003; *Vimeux et al*., 2005; *Vuille and Werner*, 2005; *Vimeux et al*., 2009; *Vuille et al*., 2012]. More recently, *Thompson et al*. [2013] also related the Quelccaya ice core δ^{18}O records to sea surface temperature in the tropical Pacific. Hence, despite being one of the most iconic paleoclimate records from the Southern Hemisphere, questions regarding its climatic interpretation remain.

The QIC and other tropical alpine glaciers are retreating in response to global warming [*Thompson et al*., 1993; *Vuille et al*., 2008; *Rabatel et al*., 2013]. Recent warming has also led to elevated freezing level heights at Quelccaya over the past half century and, at the summit, occasional above-freezing temperatures during austral summer [*Bradley et al*., 2009]. *Thompson et al*. [1993] document retreat of the QIC as well as a rise of the percolation zone, in the time between ice core drilling activities in 1976 and later in 1991. Alteration of snow δ^{18}O values by meltwater percolation has been observed at the QIC during recent decades [*Thompson et al*., 1993; *Davis et al*., 1995; *Thompson et al*., 2011]. The alteration, characterized by an increase

in the annual mean value and reduced seasonal amplitude, is associated with warming and is not evident at QIC prior to the late twentieth century [*Thompson et al*., 2011; *Bradley*, 2015]. Agreement between the QIC ice core δ^{18}O record obtained at the summit in 2003 with that obtained in 1983 indicates that despite warming and a rise of freezing level heights, the δ^{18}O record at the QIC had retained its fidelity prior to 1981 [*Thompson et al*., 1986, 2006, 2011]. Within this context, the focus of this paper is on analysis of snow-height change observations from the summit of Quelccaya since 2003, a period for which there has been no evaluation of the preservation quality of the isotope record. Therefore, the presentation in this study of monitoring and sampling results from 2003 to 2014 provides an opportunity for continued assessment of preservation quality of the QIC stable isotope record.

The QIC is positioned in the Cordillera Vilcanota of the Peruvian Andes between the Pacific Ocean and the Amazon Basin and likely records climate aspects of both regions. Quelccaya receives almost all of its precipitation during the austral summer in association with the establishment of the South American summer monsoon (SASM) over the interior of the continent. Yet several studies have documented that the moisture transport from the Amazon lowlands to the Andes in this part of the world is strongly modulated by ENSO [*Vuille et al*., 2000; *Garreaud et al*., 2003; *Vuille and Keimig*, 2004]. Upper tropospheric easterly winds, favoring moisture influx from the east, are enhanced during La Niña conditions, while the opposite pattern (strong westerly anomalies) is favored during El Niño conditions.

Here we take a first step toward using the Quelccaya stable isotope record to reconstruct the history of the SASM and to further our understanding of the climatic controls that determine the stable isotopic variability of δ^{18}O as recorded in the ice core on subseasonal to interannual time scales. A thorough understanding of the large-scale and on-site processes that determine the isotopic composition recorded in the ice will then allow us to assess whether large-scale climate phenomena, such as the SASM, have potentially left an imprint in the ice core record and could therefore be discerned and reconstructed from the Quelccaya stable isotope record. Addressing these aspects first requires a thorough analysis of the processes related to snowfall and ice formation on the ice cap today. For example, aspects of seasonality (when does snow accumulate at the summit of the QIC?) are fundamental, as stable isotopes record climate only at the time of snowfall. Postdepositional alteration of the isotopic composition of surface snow may occur and lead to erroneous climatic interpretations. Similarly, it is vital to understand the transport history and condensation processes related to moisture flux and snowfall on Quelccaya (what are the dynamics associated with snowfall at Quelccaya and what is the water stable isotopologue response associated with these dynamical conditions?).

The seasonality of stable isotopologue ratios of water vapor over the tropical Andes is characterized by more negative values during austral summer. This seasonality was recently attributed to a regime shift from large-scale advective mixing during winter to the influence of continental convection over the Amazon Basin during summer [*Samuels-Crow et al*., 2014]. However, it is not clear how the seasonality of satellite-measured stable isotopologue ratios of water vapor compares with snow δ^{18}O values on the QIC.

We are in the unique position of possessing over a decade of hourly data collected via an on-site monitoring and calibration program at the summit of the QIC. Monitoring consists of a high-elevation automated weather station (AWS) and annual snowpit sampling efforts for snow δ^{18}O measurements near the site of the Summit Dome core drilled in 2003 [*Thompson et al*., 2006]. We use AWS observations of daily snow height at the summit, translated to daily snow-height change, to (i) develop a climatology for snow-height change, (ii) to construct age models for snow δ^{18}O ratios measured from snow samples collected over the past decade, and (iii) develop regional dynamical composites for snow-height change events at Quelccaya, building on work that started more than a decade ago on Sajama Ice Cap in Bolivia [*Vuille et al*., 1998; *Hardy et al*., 2003].

The SASM is characterized by a large-scale thermally direct circulation, near-surface moisture flux onto the continent, land-atmosphere interactions related to high relief of the Earth surface, and strong seasonality of precipitation over the Amazon River Basin [*Vera et al*., 2006]. There is no seasonal wind reversal [*Ramage*, 1971]. However, compared with annual mean easterly low-level winds, austral summer wind anomalies are northwesterly and austral winter wind anomalies are southeasterly over the southwestern Amazon Basin [*Zhou and Lau*, 1998]. An upper troposphere December-January-February (DJF) anticyclone over Bolivia, the Bolivian High [*Lenters and Cook*, 1997], is maintained by Amazonia convection. The Bolivian High and the accompanying downstream trough over the Atlantic, the Nordeste Low, are remotely forced by heating

over both Africa and the tropical western Pacific [*Chen et al*., 1999; *Cook et al*., 2004]. Topographic forcing of the near-surface moist static energy (MSE) maxima, east of the tropical Andes, may also contribute to the Bolivian High [*Nie et al*., 2010]. In this convective quasi-equilibrium framework for monsoon circulations, near-surface MSE maxima occur on the poleward edge of precipitation maxima [*Arakawa and Schubert*, 1974; *Emanuel*, 1995]. At low levels, the SASM consists of the northerly South American low-level jet (SALLJ) [*Marengo et al*., 2002] and the South Atlantic Convergence Zone (SACZ) [*Carvalho et al*., 2004] belt of moisture flux convergence and convection that extends from the Amazon Basin southeast to the subtropical southern Atlantic [*Kodama*, 1992].

Precipitation regimes for the core of the SASM are (i) a low-level easterly regime associated with squall lines and a weakened SACZ [*Cohen et al*., 1995] and (ii) a westerly regime with a strengthened SACZ [*Silva Dias et al*., 2002]. Outside of the core of the SASM a rainfall anomaly dipole alternates from (i) southeastern South America when the SALLJ is strong to (ii) southeastern Brazil when low-level flow is westerly feeding moisture to the SACZ [*Nogues-Paegle and Mo*, 1997; *Boers et al*., 2014]. Precipitation over southeastern South America and the La Plata and Amazon Basins is primarily convective, although the convective systems over the Amazon Basin have a greater stratiform composition and precipitation over the oceanic SACZ is primarily stratiform [*Romatschke and Houze*, 2013].

As with other monsoons, the large-scale thermally direct circulation is accompanied by transient disturbances [*Vera et al*., 2006]. Precipitating transient disturbances include convective storms associated with the SALLJ, trade wind activity, tropical disturbances that migrate onto the continent from the Atlantic, and midlatitude cold air incursions that migrate equatorward from the La Plata to the Amazon Basins [*Garreaud*, 1999; *Vera et al*., 2006]. The latter are related to midlatitude baroclinic waves that generate a low-level southerly cold anomaly east of the Andes over Argentina. From there, convection along the north side of the cold fronts advances equatorward into the tropics [*Garreaud*, 1999]. In the context of this spectrum of precipitation mechanisms and regimes for the SASM, we find here that the heaviest of snowfall events at QIC are related to cold air incursions.

Most of the snowfall at the QIC occurs in conjunction with the SASM during the wet season and dust layers deposited during the dry season allow for dating of Quelccaya ice cores [*Thompson et al*., 1985]. Annual layers of ice are thus primarily recorders of summer precipitation. However, it remains unclear how much snowfall accumulation and preservation occurs during the winter. In this study we present a seasonal climatology of changes to the height of the snow surface at the summit of the QIC. This information may be necessary for a clear interpretation of the dry season component of the annual snow and ice layers and their δ^{18}O records.

2. Data and Methods

2.1. Data Sources

The AWS monitoring system was initially installed at the summit of QIC in 2003. Following vandalism to the equipment that year, the station was reequipped in July 2004 and has been operating since then, in harsh environmental conditions at 5680 m altitude. Measurements by the AWS include, among others, wind speed and direction, humidity, long- and short-wave incoming and outgoing radiation, air temperature, and barometric pressure. The data are transmitted by telemetry via the Geostationary Operational Environmental Satellite system. The height of the AWS system is adjusted annually during field campaigns to the summit of QIC in June or July to accommodate annual increases of approximately 2 m in snow-surface height.

Snowpits have been sampled for snow δ^{18}O annually at the summit of QIC since 2004, except in 2010, 2012, and 2013, when no isotopic data are available. Short cores were completed during sampling in 2005–2009. Prior to 2014, sample collection was typically completed during the dry season around late June to early July when snowpits were excavated to the base of the topmost annual layer. Snow samples were collected from the sidewall of the pits at 10 cm intervals, adjacent to measurements of snow density and snow water equivalent. Snow samples were shipped to Ohio State University and analyzed for δ^{18}O by mass spectrometer or the University of Massachusetts, where δ^{18}O was determined on a Picarro L2130-i Analyzer. Results are reported relative to the Vienna standard mean ocean water (VSMOW) standard and have a reproducibility of better than 0.1‰.

For assessment of precipitation and convection associated with snow-height change events at the QIC, we use the following globally gridded data sets: the Tropical Rainfall Measuring Mission (TRMM) derived 0.25° daily precipitation [*Kummerow et al*., 1998, 2000; *Huffman et al*., 2007], daily 2.5° outgoing longwave radiation (OLR) from the National Oceanic and Atmospheric Administration [*Liebmann and Smith*, 1996], and the Global Precipitation Climatology Project (GPCP) rain gauge and satellite-merged 1° daily precipitation [*Huffman et al*., 2001]. OLR, as a measure of the longwave radiation emitted by Earth's surface and atmosphere, is commonly used as a proxy for tropical precipitation as cold convective clouds reduce OLR. Hence, negative OLR anomalies (reduced energy emitted to space) indicate enhanced deep convection and vice versa. For TRMM data, we use the 3B42 Research Version from the Version 7 TRMM Multi-Satellite Precipitation Analysis algorithm.

To complement snow δ^{18}O data, we evaluate satellite-measured water vapor δD data. We use satellite observations of water vapor HDO/H_2O ratios from both the Tropospheric Emission Spectrometer (TES) and the Greenhouse Gases Observing Satellite (GOSAT). HDO/H_2O ratios are reported in the standard "delta" notation (δD) by

$$\delta D = \left(\frac{R}{R_{\mathrm{Std}}} - 1\right) \times 1000. \tag{1}$$

R is the observed ratio of heavy to light isotope and R_{std} is the ratio of the heavy to light isotope in the standard, which for hydrogen is VSMOW. TES is a thermal infrared spectrometer aboard the National Aeronautics and Space Administration's Aura satellite [*Worden et al*., 2006], and we use here the bias-corrected level 2 Version 5 Lite Product HDO and H_2O products (L2v005_litev08 [*Worden et al*., 2011, 2012; *NASA*, 2014]). GOSAT is operated by the Japan Aerospace Exploration Agency and utilizes a shortwave infrared spectrometer [*Hamazaki et al*., 2005; *Kuze et al*., 2009; *Frankenberg et al*., 2013]. TES measurements are most sensitive to the midtroposphere, while GOSAT measurements are total column integrated and therefore primarily measuring the lower troposphere where the bulk of the water vapor resides. TES HDO/H_2O observations have been used to identify large-scale mixing and moistening paths for the free troposphere [*Worden et al*., 2007; *Noone*, 2012; *Brown et al*., 2013]. Besides its applicability as a tracer for the hydrologic cycle TES data have also been useful for identifying misrepresentation of moisture in general circulation models [*Risi et al*., 2012]. Satellite observations of HDO/H_2O ratios have been used to assess the influence of monsoon convection on water stable isotopologues downstream [*Brown et al*., 2008].

Monsoon domain convection and related processes decrease stable isotopologue ratios of water vapor, and downstream advection leads to a negative relationship between precipitation stable isotopologue ratios and upstream convection. This mechanism has been used to explain the relationship between Indian monsoon convection and (i) precipitation and speleothem stable isotopologue ratios from interior northwestern China [*Lee et al*., 2012], (ii) precipitation on the Tibetan Plateau [*Gao et al*., 2013; *He et al*., 2015], and (iii) the isotopic composition of precipitation and proxy sites in the tropical Andes [*Vimeux et al*., 2005; *Vuille and Werner*, 2005; *Vuille et al*., 2012]. Similarly, austral summer water vapor δD values over the tropical Andes, which are more negative than winter values, have been linked to monsoon convection over the Amazon Basin [*Samuels-Crow et al*., 2014]. *Risi et al*. [2013] recently used both TES and GOSAT δD in their assessment of the role of continental moisture recycling on the intraseasonal variability of humidity over continents. They found winter δD variability over South America to be largely a function of continental recycling and summer δD variability over the Amazon Basin to reflect both continental recycling and convective activity. Hence, the usefulness of both of these data sets (TES and GOSAT) for assessments of moisture path histories has already been established. Here we use them as a backdrop or context for understanding variability of snow δ^{18}O at Quelccaya.

To construct dynamical composites, relating snow-height change events at the QIC with the large-scale circulation, we use the ERA-Interim reanalysis [*Dee et al*., 2011]. We use 0.7° 4 times daily surface and pressure level data of this most recent product from the European Centre for Medium-Range Weather Forecasts. Near-surface MSE was calculated using the ERA-Interim surface fields for temperature (T), specific humidity (q), and geopotential height (z), using the general equation $\mathrm{MSE} = C_pT + L_vq + gz$. C_p is the specific heat of dry air, L_v is the latent heat of vaporization, and g is the acceleration due to gravity. MSE is expressed here in kelvin (K) after dividing by C_p.

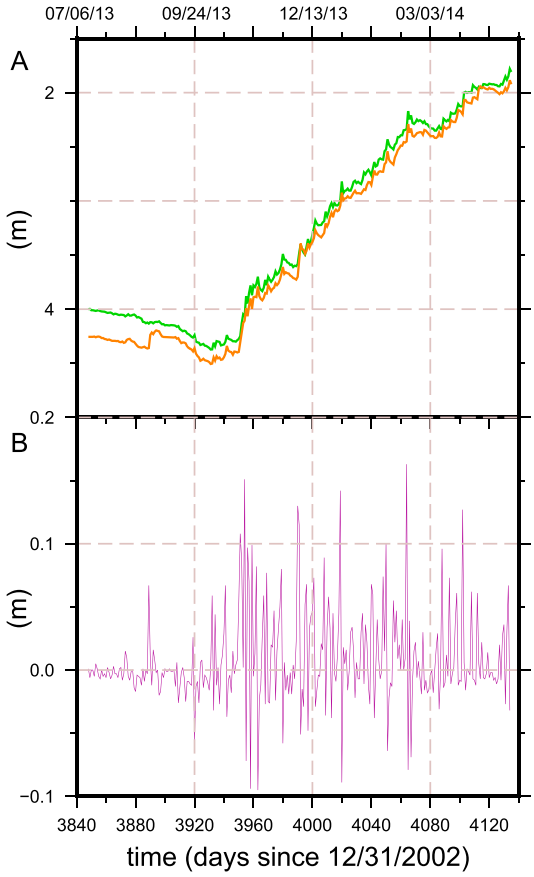

Figure 1. Daily time series of snow-height changes (m) measured by the AWS at the summit of Quelccaya Ice Cap, 14 July 2013 to 27 April 2014. (a) Distance from sensor to snow surface measured by two instruments and (b) daily average snow-height change. *X* axis indicates time (days since 31 December 2002).

2.2. Snow Height

The AWS daily snow-height change measurements collected at the QIC summit over the past decade are the foundation of this study. Two identical instruments are used to sonically measure distance from their fixed positions on the AWS tower down to the top of the snow surface. Observations are made hourly, and quality assurance protocols condense the dual instrument hourly observations to one daily average product. Instrument accuracy for hourly AWS snow-height measurements is about 0.005 m. An example of the cumulative record of the dual-instrument daily observations is shown in Figure 1a for the period from 14 July 2013 to 27 April 2014. Observations generally agree between the instruments. The two-instrument daily average snow-height change for this same interval is shown in Figure 1b. In late October of 2013 (around day 3950), both instruments recorded an interval of pronounced increase in snow height. The maximum daily snow-height change increase associated with this period is 0.15 m on 28 October 2013. Daily snow-height change values for the days preceding and following the 28th are 0.002 m and −0.07 m, respectively. Globally gridded precipitation data sets (and OLR, not shown) confirm that the anomalous snow-height change at Quelccaya is associated with region-wide convection (Figure S1 in the supporting information). The convective system migrates to the northwest, dissipates north of and a day after passing over Quelccaya, and appears to be linked to midlatitude disturbances and the SACZ to the southeast. This event helps to highlight the importance of in situ snow-height change measurements, as they allow us to relate snow-height change at Quelccaya with regional dynamics and convective systems.

2.3. Snow δ^{18}O Age Models

This section outlines the assignment of calendar dates to snow δ^{18}O records from QIC using the daily snow-height values measured near the summit. We quantitatively assign a range of dates to snow δ^{18}O sample depth intervals and in effect construct age models for snow δ^{18}O values over the past decade. Examples of the age constraint method are illustrated in Figure 2 from two snowpits, although the method was applied to short-core data as well. We begin with snow sample values per snowpit (or short core) as a function of depth interval (Figures 2a and 2b—pink lines). We tie the snow δ^{18}O record to the daily snow-height record by the sample collection date. The net sum of accumulation over the year prior to sampling is identified from the daily snow-height record (Figures 2c and 2d). This value is taken as the cumulative sum of daily snow-height change for the interval between (i) the cumulative sum minimum and (ii) the sample collection date. In Figures 2c and 2d the cumulative sum minima are the minima of the dark green lines; the right edge of the *x* axis (day 0) represents the sample collection date. Annual layer thicknesses were identified in situ as part of the sample collection procedure. We then reconcile this in situ estimation of the depth of the topmost annual snow layer with the daily snow-height record (Figures 2a and 2b—purple lines). The depth of the snowpit and the corresponding snow δ^{18}O sample depth intervals are linearly interpolated to the total thickness obtained from the daily snow-height measurements. Snowpit and snow-height change depths are compared in Table 1. The discrepancy between these depths is less than

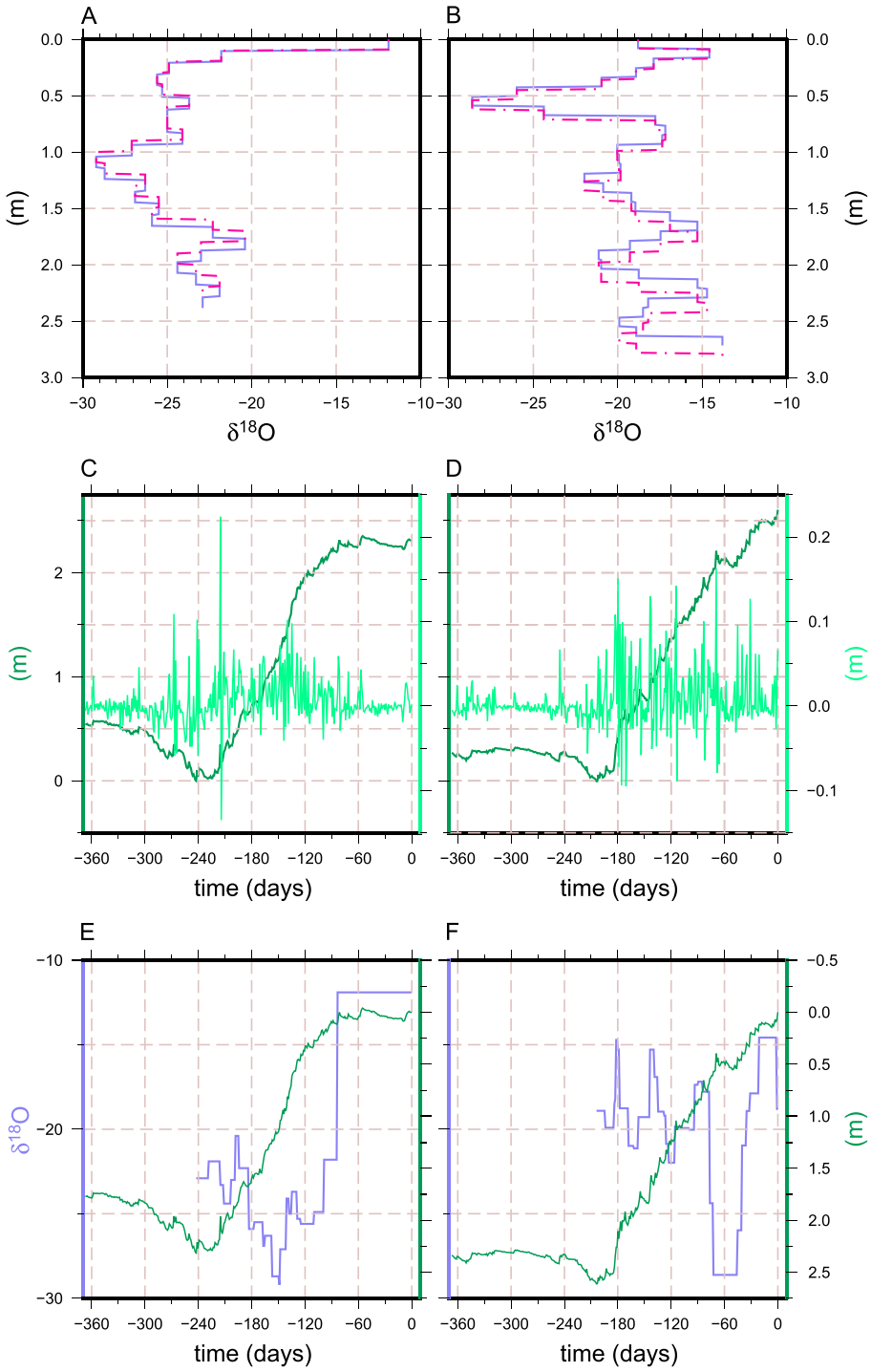

Figure 2. Age model construction for snow $\delta^{18}O$. (a and b) Snow $\delta^{18}O$ from the snowpit from the summit of Quelccaya ((left) 10 July 2011 and (right) 28 April 2014). Parameter $\delta^{18}O$ versus depth (pink dashed-dashed-dotted line) and $\delta^{18}O$ adjusted (purple solid line) to the observed AWS net snow-height change. (c and d) Daily snow-height change (light green line, right axis). Cumulative sum of the daily values (dark green solid line, left axis) referenced (as in Figure 3a) to the minimum cumulative value (~day −240 and −200, respectively). (e and f) Age model (purple solid line, left axis) for snow $\delta^{18}O$. Cumulative snow-height change (dark green solid line, right axis) is referenced to the cumulative height value on the sample day. For Figures 2c–2f, sample collection dates correspond to day zero, and the *x* axis reflects days since (negative prior) to (left) 10 July 2011 and (right) 28 April 2014.

Table 1. Hydrologic Year Snow Depth: Snowpit Depth Versus Snow-Height Change Thickness

	2004/2005	2005/2006	2006/2007	2007/2008	2008/2009	2010/2011	2013/2014
Snowpit depth (m)	2.10	2.10	2.25	2.46	1.88	2.37	2.88
Snow-height thickness (m)	1.99	2.03	2.19	2.35	1.96	2.29	2.64
Discrepancy (%)	5.5	3.5	2.7	4.7	−4.1	3.5	9.1

10% and below 5% for most years. We then conservatively assign a range of dates to sample depth intervals based on the snow-height change record (Figures 2e and 2f). For this, the snow-height change record is referenced as a depth below the cumulative snow height on the sample collection date (Figures 2e and 2f—green lines and right axes). We finally identify the range of dates over which the depth of the cumulative curve corresponds to the adjusted snow δ^{18}O sample depth intervals and assign those dates to sample values (Figures 2e and 2f—purple lines). Age models are constructed for 7 years of snowpits (2004/2005, 2005/2006, 2006/2007, 2007/2008, 2008/2009, 2010/2011, and 2013/2014) and 5 years of short cores (2004/2005, 2005/2006, 2006/2007, 2007/2008, and 2008/2009).

To augment the stable isotope analyses, we evaluate the snow δ^{18}O values, using the calendar dates derived from the above age models, against time series of satellite-observed water vapor δD from TES and GOSAT. Although we compare the hydrogen isotopic composition of water vapor with the oxygen isotopic composition from snow, there is still merit in such an exercise. Parameters δD and δ^{18}O are linked through the empirical linear relationship, described by the slope of the global meteoric water line (GMWL). The comparison allows testing of our δ^{18}O age models against the backdrop of the annual cycle of water vapor δD as well as a critical evaluation of potential postdepositional changes in δ^{18}O of surface snow.

We expect that the isotope signal of the snow at the summit of QIC is initially derived from the isotope ratio of the vapor by way of fractionation during condensation. In this context, the large-scale thermodynamic processes influencing water vapor isotope ratio distributions are important for understanding variability of snow δ^{18}O. Observations of tropical South American and Andean water vapor δD are commonly less than would be predicted by Rayleigh fractionation, and this discrepancy has been described as a product of an amount effect from upstream convection [*Brown et al*., 2008; *Samuels-Crow et al*., 2014]. DJF air parcel trajectories from the western Amazon Basin and Quelccaya principally track to the Amazon Basin and further upstream (east) to the Atlantic. It is however noteworthy that some trajectories also track south/southeast to subtropical and southern South America, such as would be expected from cold air incursions [*Brown et al*., 2008; *Samuels-Crow et al*., 2014].

2.4. Regional Composites

For reference, a summary of South American DJF climatology for the variables of interest is presented in section S1 and Figure S2 in the supporting information. Regional DJF composites were constructed for a suite of percentile bins from the QIC daily snow-height change values. We consider upper 90th percentile bins, 60th to 90th percentile bins, 30th to 60th percentile bins, and lower 30th percentile bins, positive and negative (Figure 3b). Composites were computed for the following observed and reanalysis fields: precipitation, OLR, near-surface MSE, column-integrated water vapor flux, horizontal wind, and geopotential height. Student's *t* tests were completed for field composites, and only values that are significant at the 95% level are shown. Composites for an extended summer season (not shown), October through April, are qualitatively similar to the composites presented here. Additional details of the compositing method are presented in section S2.

3. Results

3.1. Snowfall Characteristics on QIC

A summary of more than a decade of snow-height change observations from the summit of QIC is presented in Figure 3. Interannual variability can be seen in Figure 3a by comparing the different curves of the cumulative sums of daily snow-height change measurements for each year. The distribution of *y* values at the right side of the curves in Figure 3a indicates that the total annual accumulation varies between about 1.6 to 2.6 m. Note that unlike Figure 1a, where the distance from sensor to the snow surface was plotted and hence snow-height increase results in lower values, here in Figure 3a we show values of snow accumulation/ablation. Values are referenced to

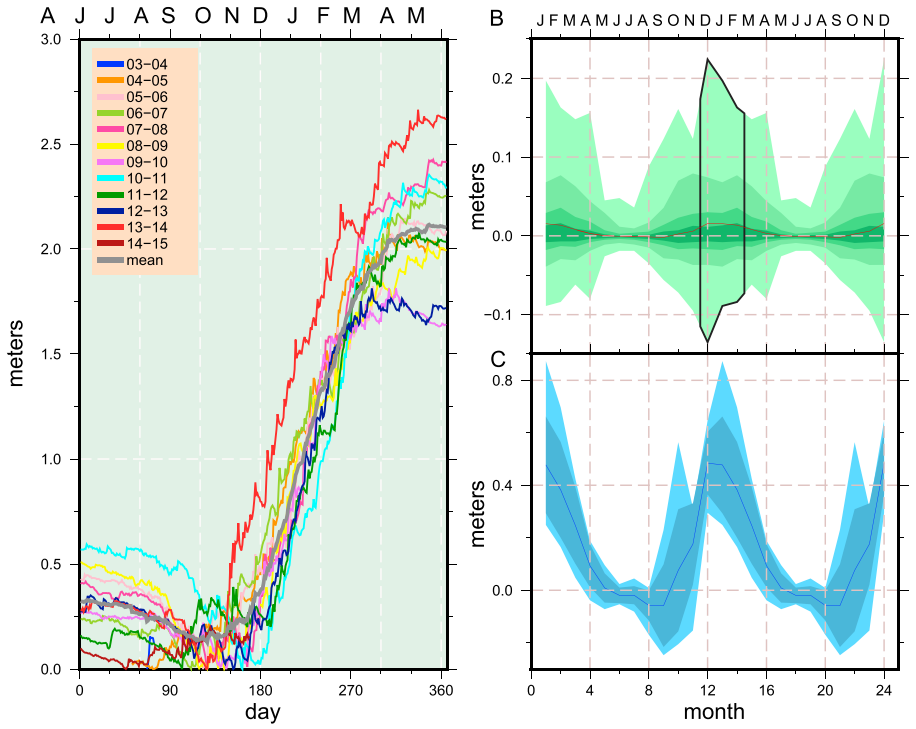

Figure 3. Distribution of snow-height change values measured with the AWS at Quelccaya Ice Cap, Peru (2003–2014). (a) Cumulative sum of daily snow-height changes. Individual annual hydrologic cycles June through May (day 0 = May 31) are distinguished by color with the 11 year mean in gray. Values are referenced ($y = 0$) to the minimum cumulative value per hydrologic year (June–May). (b) Monthly distribution of daily snow-height change values at QIC, by percentile bin. The shading indicates the percentile bin, with darkest to lightest shading corresponding with lowest (30th) to highest (90th) percentile bins, respectively. Also shown are the 30th to 60th percentile bins and the 60th to 90th percentile bins. The monthly mean daily value is indicated by the solid red line. The solid black line outlines DJF. (c) Distribution of monthly net snow-height change values, mean = blue line, mean plus and minus one standard deviation = dark blue shading, and the full range of monthly values = light blue shading. The annual cycle is doubled along the x axis in Figures 3b and 3c to center the figure on the wet season, months 12 and 24 = December. Top time axes are labeled with month initials.

the lowest cumulative value observed per hydrologic year (June through May; $x = 0$ for 31 May). Annual increase of snow height is on average about 1.8 m, accounting for the snow-height loss that precedes wet-season onset. Maximum wet-season snow-height increase occurred during the 2013–2014 hydrologic year when snow height increased by more than 2.6 m. This anomalous wet season began with the pronounced snow-height increase event of late October 2013 (Figure 1 and Figure S1), suggestive of a relationship between timing of wet-season onset and annual net snow-height gain at QIC. Later in this section we discuss the interannual correlation between the duration of the wet season and the amplitude of snow-height change at QIC.

The focus of this paper is on snow-height observations, representing accumulation of snow, rather than on precipitation in water equivalent; our use of the term snowfall refers to the resulting change in surface height at our AWS. We emphasize height change because (1) the ice core record is developed only from the net accumulation of snow and (2) high-frequency density measurements (i.e., daily or event based) are not available. Detailed density profile measurements made during field campaigns reveal that the interannual variability of bulk density (i.e., net snow accumulation) varies only slightly (mean = 448 ± 25 kg m^{-3}; $n = 6$, $r = 0.96$). In addition, thermal homogeneity at Quelccaya summit likely accounts for the minimal intraannual variability in snowpit density. Consequently, net water-equivalent accumulation and net snow-height change show a strong and consistent positive relationship at the summit. Also, we note that snow-height change is likely to be a more accurate measure of ice core accumulation than data from a notoriously unreliable precipitation gauge (if available). References to accumulation hereafter refer to positive cumulative tendency of snow height.

Monthly distributions of daily snow-height change values are shown by percentage bin in Figure 3b. Positive snow-height change days occur throughout the year, with the largest-magnitude events occurring in austral

Table 2. Interannual Correlation Coefficients Between Hydrologic Year (June Through May) Net Snow-Height Change and Parameters Listed in the Table

	Wet-Season Snow-Height Change	Duration	Onset	Decay
r	0.89	0.71	−0.54	0.41
r^2_{adj}	0.76	0.44	0.21	0.07
P value	0.001	0.021	0.10	0.24

summer. For the period of record, 2004 through 28 April 2014, net snow-height increase has been 18.03 m, about 70% of which occurs during DJF. The total DJF snow-height increase is 5.50 m, 7.85 m, 3.55 m, and 1.08 m for the positive 90th, 60–90th, 30–60th, and 0–30th percentiles, respectively. The most pronounced negative daily snow-height values also occur in austral summer. It is not uncommon for the largest positive snow-height change events to be immediately followed by a day of negative snow-height change, likely reflecting settling, wind-scour, and compaction of newly fallen snow. Sublimation and melt likely play a role though and account for other negative daily snow-height change values.

Average net monthly snow-height increase at QIC peaks during DJF (solid blue line, Figure 3c): about 0.49 m, 0.48 m, and 0.40 m for December, January, and February, respectively. Average net monthly snow-height change is negative May through September. Outside of the December-January-February (DJF) season, the standard deviations of net monthly snow-height change values are greatest in October (0.23 m), September, and November (both above 0.15 m). Standard deviation of net monthly snow-height change at the end of the wet season, April and May, is low (0.08 m and 0.06 m). These findings suggest that the duration of the snow-height gain season and the magnitude of accumulation are likely to be more influenced by snow-height change events during September-October-November (SON) in the early parts of the wet season, compared with April–May events at the end of the summer season.

To assess interannual variability, we consider the 10 years of AWS-observed yearly snow-height changes at QIC compared with durations of the season when snow-height change is positive. Correlation coefficients (r), adjusted r^2 values (r^2_{adj}), and P values between the hydrologic year (June–May) net snow-height gain at QIC versus wet season snow-height gain, accumulation season duration, snow-height gain onset date, and snow-accumulation decay date are summarized in Table 2 and Figure 4. Although the period of record is short (10 years) for statistical analysis of annual values, the relationships are in the expected direction; long wet season, early onset, and late decay correspond with greater net snow-height increase at QIC. The annual cumulative curves of Figure 3a are referenced to the minimum cumulative value per year ($y = 0$). Onset is defined, in this simple approach, as the number of days between the end of May ($x = 0$ for May 31) and the reference day (i.e., when $y = 0$ in Figure 3a). Onset dates range from day 73 to day 153 ($\mu = 127$, $\sigma = 27$ days), since the end of May, corresponding to early August to late October. Decay is defined as the date of the maximum cumulative sum of daily snow-height change values or the maximum values in each of the curves in Figure 3a. Decay dates range from 291 to 352 days since the end of the prior May ($\mu = 330$, $\sigma = 21$ days), corresponding to

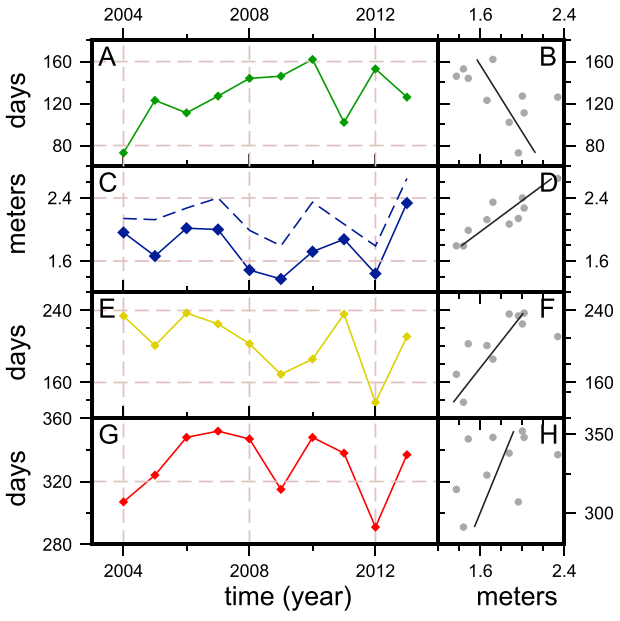

Figure 4. Interannual snow-height change time series (left; 2004/2005–2013/2014) and correlations (right) with net annual snow-height change (solid blue line in Figure 4c), (a and b) for snow-height gain onset date, (c and d) wet-season snow-height gain (dashed blue line in Figure 4c) in meters, (e and f) accumulation season duration in days, and (g and h) snow-accumulation decay date. In Figure 4c, the solid line and symbols are the net annual snow-height gain, and the dashed line is the wet-season snow-height gain in meters. The solid lines at the right are best fit lines corresponding to r values provided in Table 2.

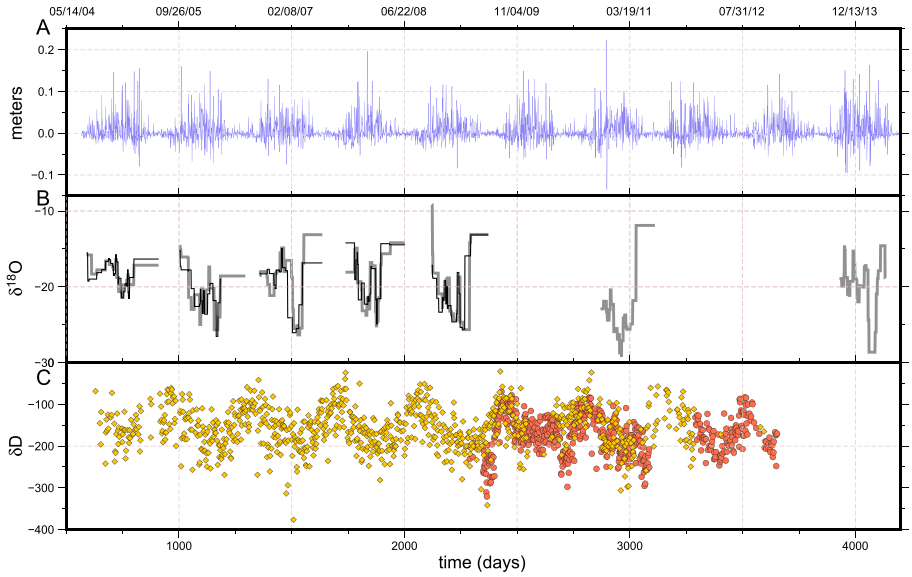

Figure 5. (a) Time series of daily snow-height change (meters) at the summit of the Quelccaya Ice Cap, mid-2004 through April 2014. (b) Time series of snowpit (thick gray) and short-core (thin black) snow δ^{18}O (per mil, right axis). (c) Satellite-observed water vapor δD (per mil) from TES (gold) and GOSAT (orange). The *x* axis is time, days since 31 December 2002, beginning at day 500.

mid-March to mid-May. Values for the duration of the accumulation season (decay minus onset dates) range from 138 to 237 days ($\mu = 203$, $\sigma = 32$ days). Net annual snow-height gain is the sum of daily snow-height change values for the entire hydrologic year, June through May ($\mu = 1.78$, $\sigma = 0.30$ m). (Note that these values differ from those of the second row of Table 1 (with an average of about 2.1 m), where we compared net snow-height change, onset (approximately early October) through the following May 31, to annual snowpit depths completed commonly in June.) Wet season snow-height gain ($\mu = 2.15$, $\sigma = 0.26$ m), which differs in that it is the sum of daily snow-height change from onset to decay, is correlated with net annual snow-height gain (Figures 4c and 4d). We interpret this to indicate that interannual variability of net snow-height gain at QIC is primarily a function of the amount of snowfall in the wet season, rather than snow-height loss during the dry season.

In summary, net snow-height gain at QIC occurs only during austral summer and particularly during DJF. There is a net decrease in snow-height during austral winter, implying that the ice core record from QIC likely does not record isotope ratios that are telling of precipitation throughout the year but rather only of the wet season (approximately October through April). In fact, the late wet-season snow-height increase is subsequently removed during the dry season as well, when net lowering of the snow surface occurs. Hence, the Quelccaya ice core δ^{18}O record is highly seasonally biased, recording almost exclusively wet-season accumulation and large-scale climatic conditions. The record may be modified somewhat during the dry season and therefore cannot represent an annual mean climate. This is important when considering the paleoclimate record from QIC. Interannual variability of snow-height change is tied to snowfall in the wet season, not loss of snow-height during the dry season. Longer accumulation seasons ($P < 0.05$) and earlier accumulation onset ($P <= 0.10$) contribute significantly to greater annual snow-height increase at QIC, while the decay date is not significantly correlated.

3.2. Stable Isotopes

As previously discussed, positive snow-height change near the summit of QIC occurs primarily during austral summer, coinciding with the SASM season. This seasonal cycle can be seen in the more than a decade long time series of daily snow-height change observations in Figure 5a. Snow δ^{18}O age models, constructed for 7 years of snowpits and 5 years of short cores, are shown in Figure 5b. There is a fair degree of agreement ($r = 0.74$, $P < 0.01$) between the complementary records of snowpit and short-core snow δ^{18}O. For reference and comparison, atmospheric water vapor δD values, from satellite observations near QIC, are also plotted in Figure 5c.

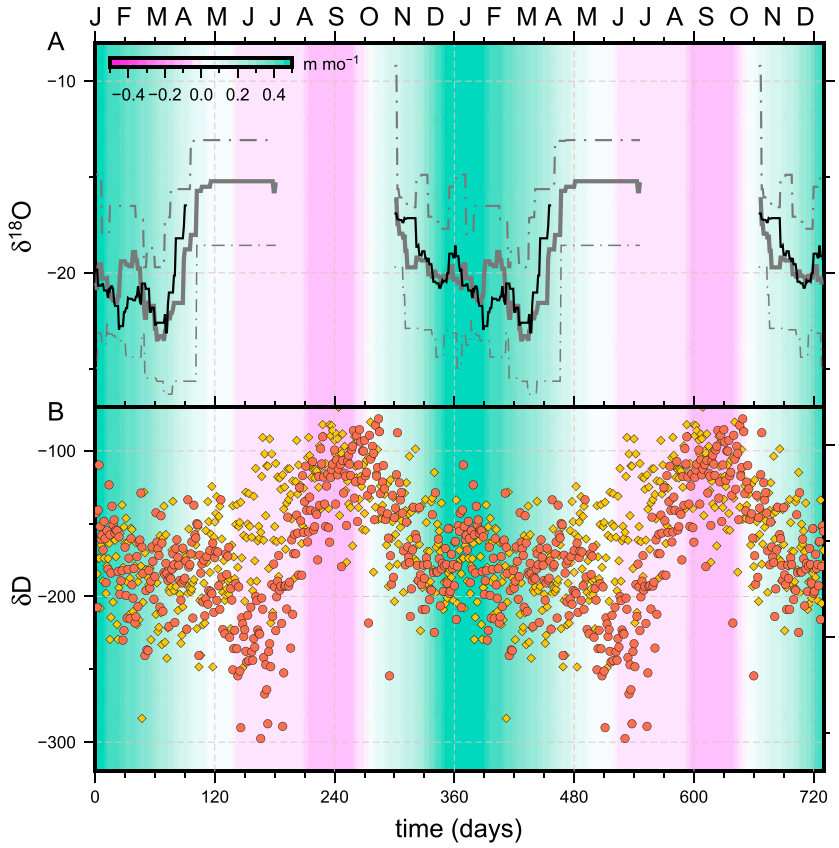

Figure 6. Climatologies (seasonal cycle) of (a) snow and (b) atmospheric water vapor stable isotope ratios. For reference, the color shading indicates the average net monthly snow-height change (as in Figure 3c). (Figure 6a) Years 2004–2014 mean snowpit (solid gray) and short-core (solid black) snow δ^{18}O ratios. The range of snowpit δ^{18}O values is indicated by the gray dash-dotted line. (Figure 6b) Satellite-observed atmospheric water vapor δD (per mil; TES—gold; GOSAT—orange) daily values (symbols) for Quelccaya.

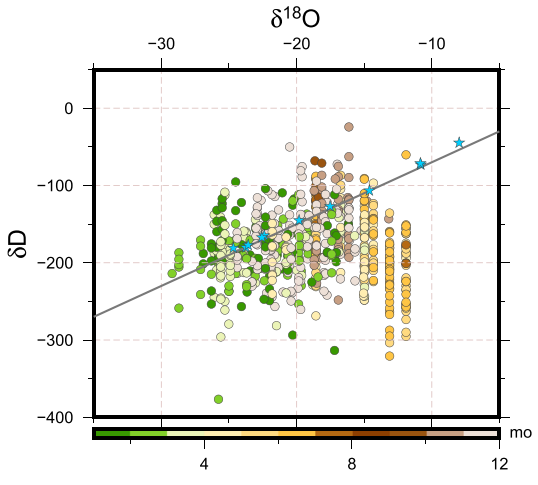

Figure 7. Distribution of snow δ^{18}O (per mil) versus satellite-measured water vapor δD (per mil). The global meteoric water line is shown for reference ($\delta D = [8 \times \delta^{18}O] + 10$). The circle shading indicates the calendar month, January = 1. The blue stars are the GNIP data for Nunoa, Peru (−70.63°S, −14.5°S; 4135 m altitude).

The first-order trend of both austral summer snow δ^{18}O and vapor δD values is decreasing through the SASM season, from about late October to mid-March (Figure 6, days ~300 to 440). Snow δ^{18}O and vapor δD maxima do not temporally coincide, and we interpret this offset to reflect (i) negative net snow-height change in austral autumn winter and (ii) postdepositional alteration, during the dry season, of late wet-season snow δ^{18}O.

Water vapor δD does not abruptly increase at the end of the SASM season, in contrast with snow δ^{18}O which abruptly increases at the end of the accumulation season. In fact, water vapor δD above Quelccaya continues to decrease until June (day ~150–180), 2–3 months after snow accumulation on Quelccaya typically stops. Hence, the very negative satellite vapor δD values are not recorded in the snow of the QIC since average net monthly snow-height change at QIC is negative from May through austral winter (Figure 6, magenta shading).

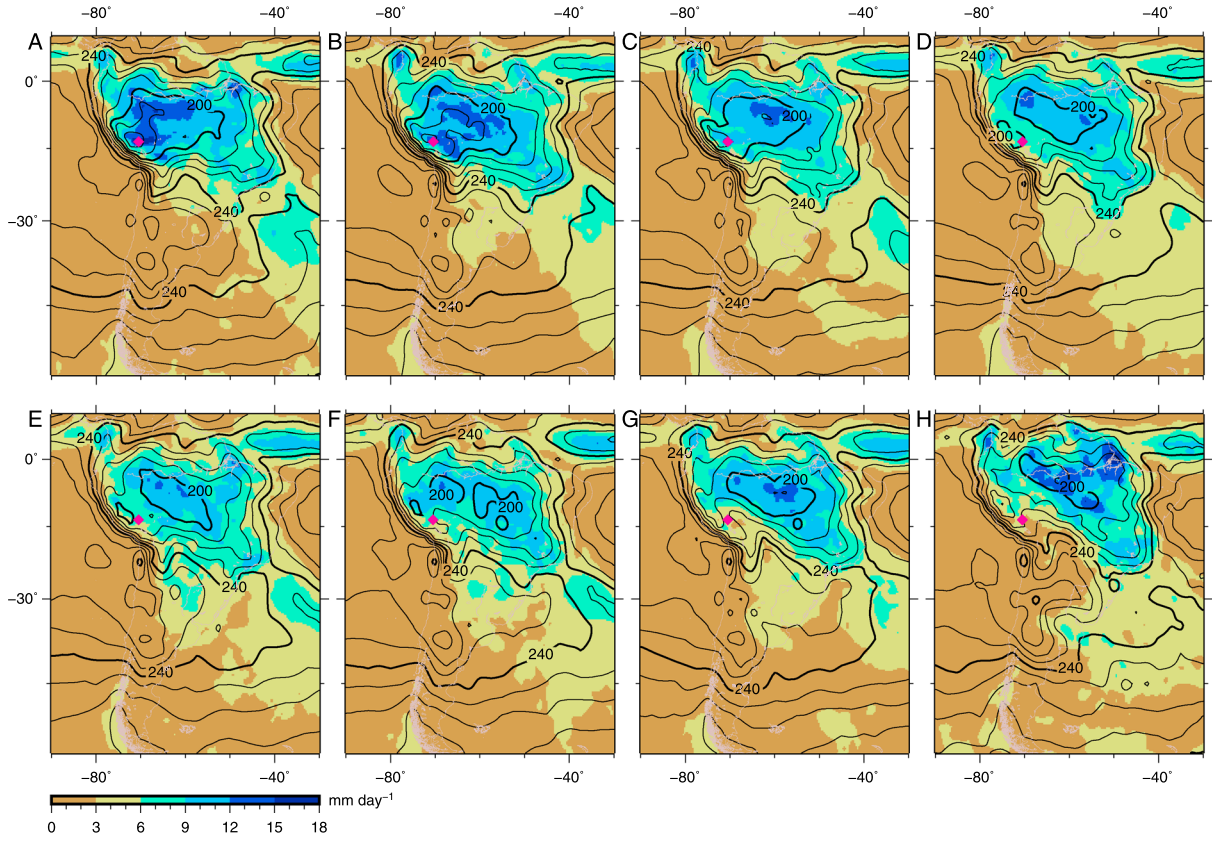

Figure 8. DJF precipitation (shaded, mm d^{-1}) and outgoing longwave radiation (contours, interval (bold) = 10 (40) W m^{-2}) composites for (top) positive and (bottom) negative snow-height change percentile bins for QIC, DJF. (a) Positive 90th percentile; (b) positive 60th–90th percentile; (c) positive 30th–60th percentile; (d) positive 30th percentile; (e) negative 30th percentile; (f) negative 30th–60th percentile; (g) negative 60th–90th percentile; (h) negative 90th percentile.

It follows that water vapor δD reaches its annual minimum at the same time as snow data on Quelccaya exhibit its most enriched values. We interpret this contrast to reflect a postdepositional alteration of late summer snow δ^{18}O to higher values, as a result of the loss of the lighter oxygen isotope during the austral winter [e.g., *Ginot et al.*, 2001, 2006; *Stichler et al.*, 2001; *Winkler et al.*, 2009].

The joint distribution of snow δ^{18}O and vapor δD values compared with the slope of the GMWL further suggests that postdepositional processes elevate surface snow δ^{18}O values during the dry season (Figure 7). Data are not currently available for a Quelccaya local meteoric water line. Therefore, in Figure 7, we include values for a high-altitude (4135 m) Global Network of Isotopes in Precipitation (GNIP) site (GNIP Station Code 8471002) that is nearby (−70.63°W, −14.50°S) and for which there is both δ^{18}O and δD data [*International Atomic Energy Agency/World Meteorological Organization*, 2015]. The distribution of these data for Nunoa, Peru (Figure 7, blue stars with a slope of 8.19), suggests that precipitation δ^{18}O and δD of the central Andes are consistent with the GMWL. The Quelccaya distribution (Figure 7, circles) of snow δ^{18}O and vapor δD values, particularly for those pairs from the near-surface with δ^{18}O less than about −16‰, approximate the slope of the meteoric water lines with a slope near 8. Quelccaya samples during May and June with δ^{18}O of −16‰ or greater, however, are offset from the meteoric water line, in that δD is less than (or δ^{18}O is more than) the meteoric water line. This is indicative of disequilibrium evaporative loss. Kinetic effects such as postdepositional sublimation of surface snow after the wet season has ended, readily explains the −100‰ δD displacement of late wet-season pairs of values below the GMWL [*Gat*, 1996].

3.3. Regional Composites

There is a systematic correspondence between the magnitude of snow-height change at Quelccaya, regional precipitation, near-surface MSE, and OLR. High-magnitude positive snow-height change at QIC corresponds

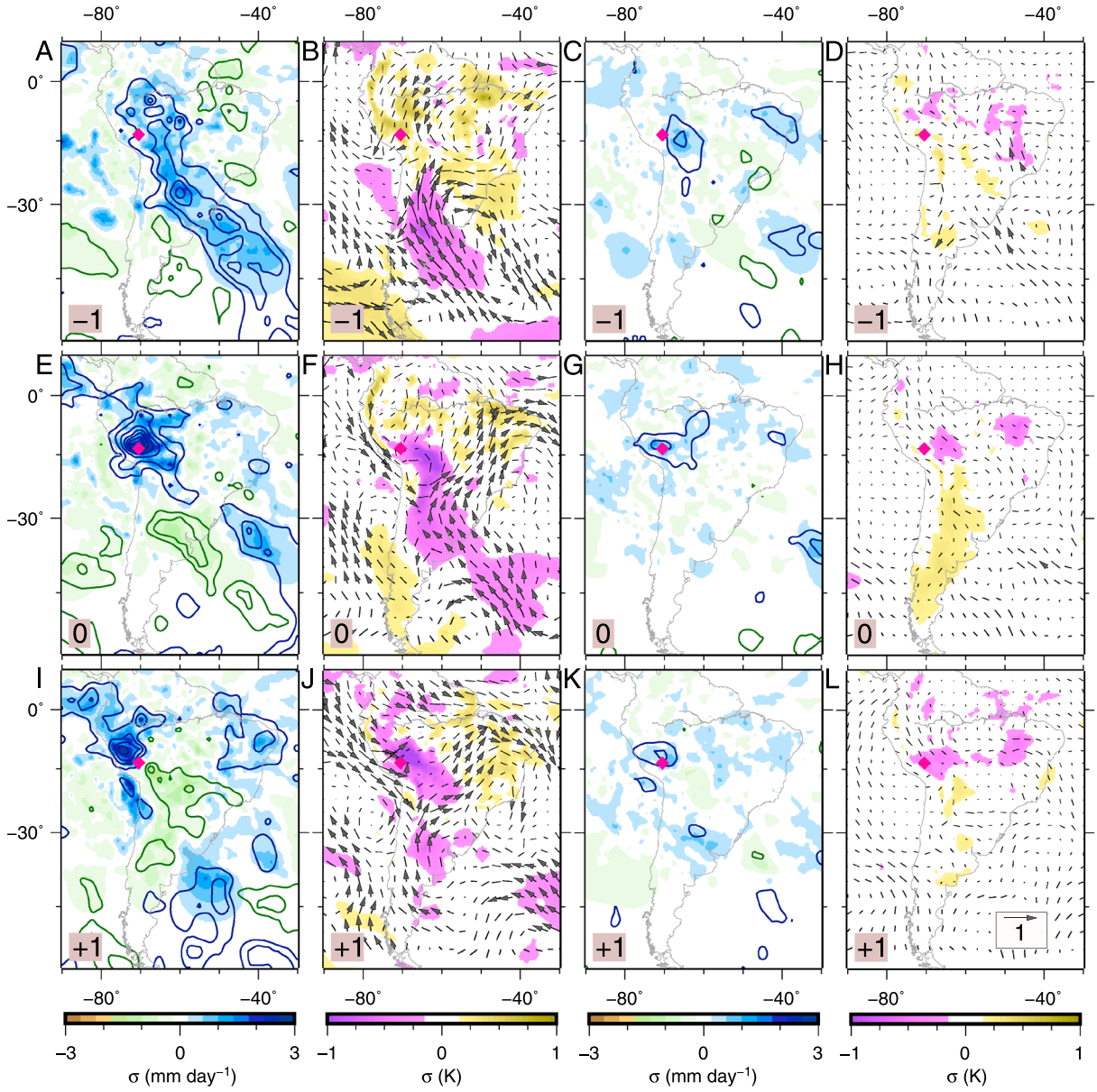

Figure 9. Lead-lag anomaly composites for positive snow-height change events at QIC, DJF at (a–d) −1, (e–h) 0, and (i–l) +1 day. (first column) Precipitation (shaded) and outgoing longwave radiation (contours, negative blue, positive green, interval = 0.4 sigma) for 90th percentile. (second column) Near-surface moist static energy (shaded) and column-integrated water vapor flux (vectors) for 90th percentile. (third column) Same as in first column but for the 30–60th percentile and (fourth column) same as in second column but for the 30–60th percentile. Anomalies are normalized by the standard deviation (σ, sigma) of DJF values. For reference, the units of the shaded fields prior to standardization are shown in parentheses below the colorbars. A 1σ scale vector is shown in Figure 9l.

with precipitation maxima and OLR minima concentrated over the western Amazon Basin and the central Andes (Figures 8a and 8b). This result clearly indicates that intense snowfall events on Quelccaya are not of a local origin but coincide with enhanced precipitation over much of the western and central Amazon Basin. Moderate- to low-amplitude snow-height change at QIC corresponds with precipitation and OLR patterns that are similar to the DJF mean (Figures 8c–8f). High-amplitude snow-height loss at QIC corresponds with precipitation and OLR maxima concentrated over the lower reaches of the Amazon River and eastern-northeastern Brazil and secondary precipitation maxima over the Brazilian Highlands (Figures 8g and 8h). These patterns of precipitation and OLR importantly distinguish the decade-long daily snow-height change record from QIC as an indicator of convection and precipitation over the entire SASM domain.

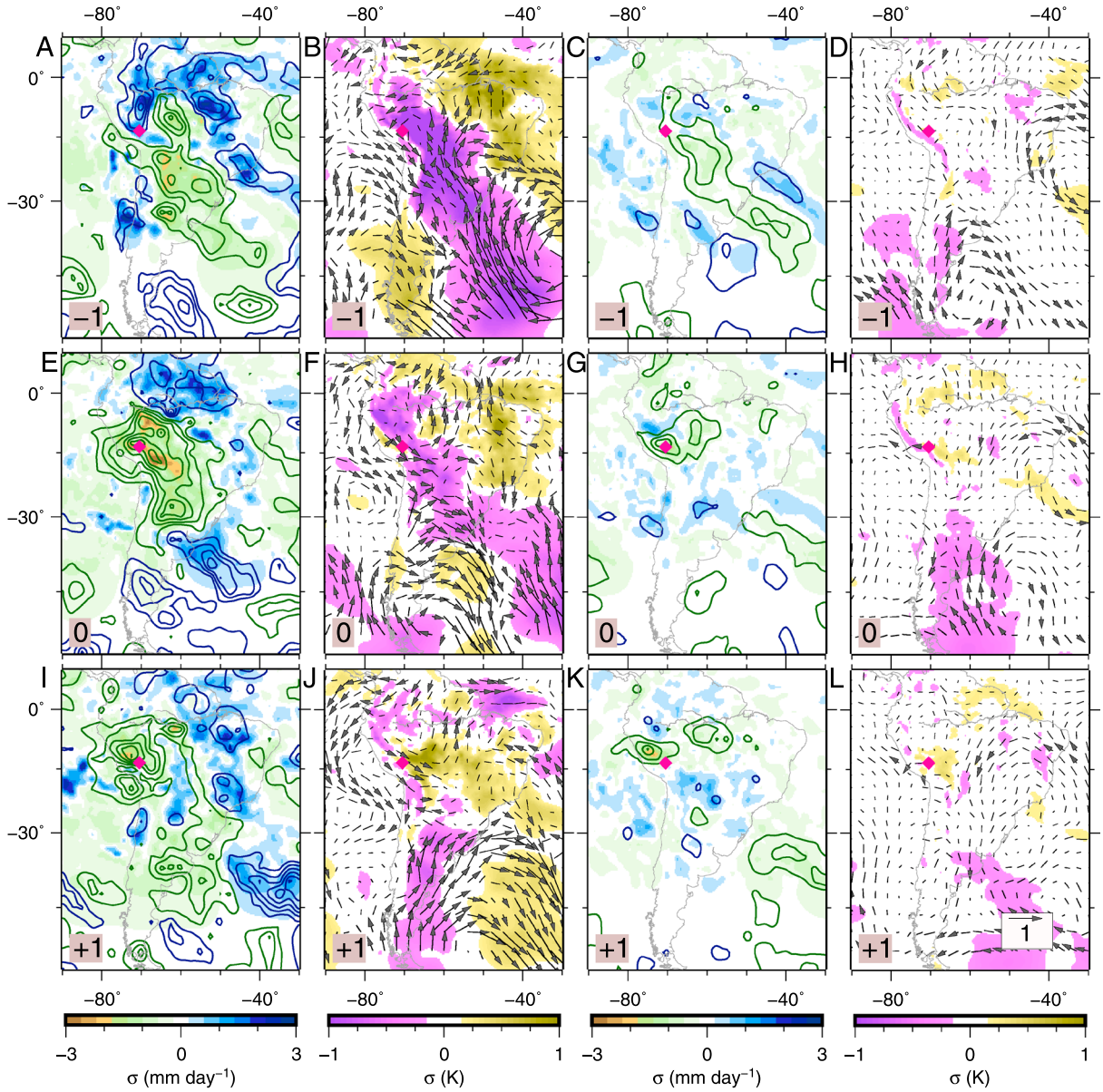

Figure 10. Same as in Figure 9 but for negative snow-height change percentiles.

To assess dynamical aspects of the snow-height change percentile bin composites, we present lead-lag anomaly composites for high-amplitude QIC snow-height change events (Figures 9 and 10 and Figure S3). Precipitation, OLR, and near-surface and lower troposphere moist dynamics are presented in Figures 9 and 10. For brevity, we present the lead-lag analyses for the high- (90th) and moderate- (30^{th}–60th) amplitude positive (Figure 9) and negative (Figure 10) snow-height change events. Analysis of upper troposphere circulation anomalies (Figure S3) suggests that the amplitude of snowfall at Quelccaya is not simply in response to Bolivian High activity as Bolivian High activity is modulated by extratropical wave trains [*Vuille and Keimig*, 2004].

Positive 90th percentile (and 60th–90th percentile; not shown) events at QIC correspond with northwestward advection of a near-surface negative MSE anomaly, positive precipitation, and negative OLR anomalies. Over 2 to 3 days, a continental precipitation anomaly maximum and OLR anomaly minimum track from the upper Rio de la Plata to central Peru, along the equatorward edge of an advancing cold front (Figures 9a, 9e, and 9i).

The cold front is along the equatorward edge of the negative near-surface MSE anomaly (Figures 9b, 9f, and 9j). Negative MSE anomalies here indicate cold and dry air. Southerly water vapor flux anomalies are accompanying

the cold front (Figures 9b, 9f, and 9j). We interpret these systems as cold air incursions, which are episodic surges of cold extratropical air into subtropical South America on the lee side of the Andes that occur throughout the year at a period of about 10 days [*Garreaud*, 2000]. During summer, incursions are characterized by convection along their equatorial fronts into the Amazon River Basin [*Garreaud and Wallace*, 1998; *Vera and Vigliarolo*, 2000; *Li and Fu*, 2006].

The northward propagation of convection associated with these systems liken them to the Type 1 cold-frontal incursions of *Siqueira and Toledo-Machado* [2004] and *Siqueira et al*. [2005]. In austral winter, incursions that penetrate into tropical latitudes, specifically the western Amazon Basin, are characterized by particularly anomalous low-level southerly winds [*Espinoza et al*., 2013], not unlike patterns we observe in austral summer (Figures 9b, 9f, and 9j). Deep convection over the southwestern Amazon Basin is accompanied by anomalous divergence in the upper troposphere (Figure S3c). Most of the net snow-height gain at Quelccaya is from these cold air incursions as ~70% of the height gain is from the positive 90th and 60–90th percentile bins combined.

Moderate-amplitude (and low amplitude; not shown) snow-height gain at QIC is related to isolated mesoscale convective systems not associated with southerly cold air incursions (Figures 9c and 9d, 9g and 9h, and 9k and 9l). Near-surface MSE anomalies for the lower amplitude snow-height gain events are positive over southern South America and negative over the Amazon (Figure 9h). We interpret these as comparable to *Rickenbach et al*.'s [2002] "non-SACZ" regime characterized by smaller-scale mesoscale convection over the southwestern Amazon Basin.

Negative 90th percentile (and 60th–90th percentile; not shown) snow-height change events at QIC are characterized by a positive OLR anomaly (and negative precipitation anomaly) that extends over much of the southwestern Amazon Basin (Figures 10a, 10e, and 10i). Near-surface MSE anomalies for these systems are intensely negative over the approximate mean location of the SACZ and positive north and east of there with maxima over the mouth of the Amazon River and northeastern Brazil (Figures 10b, 10f, and 10j). This pattern resembles the terminus of the cold air incursion events, with low-MSE air propagating northwest behind a cold front and a positive precipitation anomaly. There is anomalous westerly moisture flux over the central Andes feeding into the dry zone of the western Amazon Basin, suggesting enhanced westerly advection of dry eastern Pacific air over the central Andes during these events. This association between westerly Pacific flow and dry episodes [*Garreaud et al*., 2003] is consistent with *Chou and Neelin*'s [2001] "ventilation" of low-MSE air from the Pacific [*Garreaud et al*., 2003] as a modulator of the position of continental convection over South America. In the upper troposphere, these systems are characterized by a low geopotential height anomaly tied to the eastward propagating extratropical cyclone over the southern Atlantic (Figures S3b, S3d, and S3f). There is anomalous upper tropospheric convergence over the southern Amazon, consistent with the negative near-surface MSE anomaly.

Moderate-amplitude (and low amplitude; not shown) snow-height loss at QIC corresponds with northwestward propagating dry zones (Figures 10c, 10g, and 10k), local negative MSE anomalies over the northern and central Andes, and local positive MSE anomalies over the southwestern Amazon Basin (Figures 10d, 10h, and 10l). The local nature of the near-surface MSE anomalies suggests that low-amplitude snow-height loss may reflect thermal dynamics associated with the orography of the Andes.

In summary, high-amplitude snow-height change at QIC, positive and negative, is related to cold air incursions of extratropical air into the Amazon Basin. Equatorward of the incursion fronts, positive precipitation and negative OLR anomalies are advected equatorward from southern South America toward the QIC on days of high-amplitude snow-height gain. Behind the incursion fronts, negative MSE, positive OLR, and negative precipitation anomalies follow the convection and pass over the QIC on days of high-amplitude snow-height loss.

In general, anomalies are advected from the east-southeast (Paraguay, southern Brazil, and Bolivia) to the west-northwest (Peru and the western Amazon Basin). This is true for both snow-height gain and snow-height loss events at QIC. The advection trajectory of the anomalies is in-line with the orientation of the SACZ, suggestive of upstream propagation of the anomalies, at least in the context of a northerly-northwesterly summer mean flow.

The regional composite patterns suggest that the magnitude of snow-height change at QIC is tied to ventilation of the monsoon domain. Ventilation in this context refers to a variation of the ventilation mechanism of *Chou et al*. [2001] and *Chou and Neelin* [2001, 2003], whereby the exchange of MSE between the warm and humid

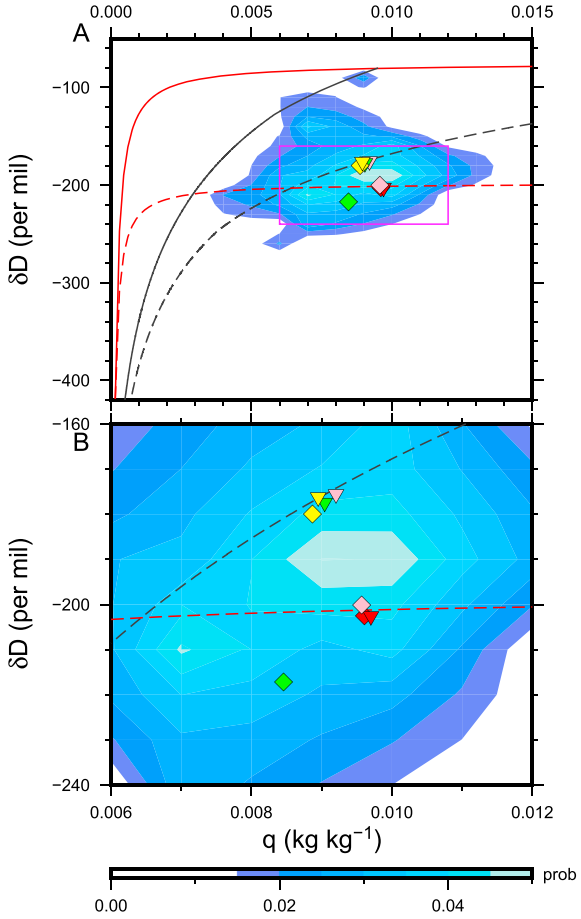

Figure 11. Joint distributions of satellite-measured water vapor q versus δD (TES). Distribution of DJF long-term mean (shaded) and median positions of snow-height change percentile bins (symbols). Red diamond–positive 90th percentile; red inverted triangle–positive 60th–90th percentile; pink diamond–positive 30th–60th percentile; pink inverted triangle–positive 30th percentile; yellow inverted triangle–negative 30th percentile; yellow diamond–negative 30th–60th percentile; green inverted triangle–negative 60th–90th percentile; green diamond–negative 90th percentile. The magenta box in Figure 11a outlines the area for the zoom-in shown in Figure 11b. Rayleigh fractionation (black lines) shown for reference with initial vapor δD of −80‰. Rayleigh curves begin at the upper right with a temperature of 280 K (solid) and 305 K (dashed). The mixing lines (red) are shown for mixing between (i) a dry end-member (q = 0.00015 kg kg^{-1}; δD = −420‰) and (ii) a vapor in equilibrium with an ocean source (solid, δD = −80‰) or a vapor whose δD has been lessened (dashed, δD = −200‰) by convection since evaporation from an ocean source.

monsoon domain and low-MSE air of, in this case, the extratropics determines the poleward limit of the monsoon circulation [*Hurley and Boos*, 2013]. High-amplitude snow-height gain at QIC corresponds with convection over the southwestern Amazon Basin, reduced ventilation and reduced export of energy from the monsoon domain to the extratropics. In the absence of a cold air incursion, the SALLJ ventilates the monsoon domain exporting high-MSE air into the extratropics.

3.4. Water Vapor Isotopologues

There is a systematic correspondence between the direction and amplitude of snow-height change at QIC and the joint distributions of q and water vapor δD in the vicinity of QIC (Figure 11 and Figure S4). The distribution of DJF q and water vapor δD near the QIC (Figure 11 shading) is centered at around 0.009 kg kg^{-1} and −190‰, consistent with DJF Amazonia distributions of both *Brown et al.* [2008] and *Samuels-Crow et al.* [2014]. When snow-height change is negative and the OLR anomaly is positive at QIC, then the joint distribution of q and δD approximates Rayleigh conditions (green inverted triangle and yellow symbols of Figure 11 and Figures S4e–S4g). Humidity is lower, and δD tends to be higher than mean summer values. When snow-height change is positive at QIC, and there is convection in the vicinity of Quelccaya, humidity values are higher and δD values are lower than both Rayleigh curves and the mean DJF values (Figure 11 and Figures S4a–S4c). The enhanced moisture and lessened δD values during snow-height gain at QIC are generally interpreted to reflect the "amount effect" associated with intense convection and "super-Rayleigh" distillation [*Noone*, 2012; *Brown et al.*, 2013]. This displacement of tropical South American water vapor values below the Rayleigh curve (Figure 11) has been tied to Amazonia convection [*Brown et al.*, 2008; *Samuels-Crow et al.*, 2014]. Here we show that some of the displacement of summer South American q and water vapor δD distributions below the Rayleigh curves is related to intense convection of cold air incursions. Similarly, negative δD anomalies associated with large-amplitude snow-height loss in the wake of cold air incursions (Figure 11, green diamond—negative 90th percentile) may reflect super-Rayleigh distillation. Large-scale mixing may also play a role, if we consider mixing between a dry end-member and a vapor δD value lessened by convection after evaporation from an ocean source (Figure 11, dashed mixing line, pink diamond, and red symbols). Low-vapor δD values of potential dry end-members may be associated with the extratropical cold air incursions, consistent with recent observations in the Andes of low-vapor δD during intrusion and cold air outbreak events [*Galewsky and Samuels-Crow*, 2014; *Galewsky*, 2015].

3.5. Summary of Results

Based on a decade of hourly snow-height observations at the summit of QIC, annual snow-height increase is about 1.8 m (~0.8–0.9 m water equivalent). The largest-amplitude daily snow-height change events occur during austral summer in accord with the SASM season. Average net monthly snow-height gain is greatest in DJF and negative May through September. The isotopic record contained within Quelccaya's ice is predominantly a history of austral summer climate, although the degree of postdepositional alteration and other parameters such as dust of course give additional information on austral winter climate. Interannual variability of snow-height gain at the summit of QIC is tied to snowfall during the wet season, rather than the amount of snow-height loss that occurs during austral winter. Longer wet seasons and earlier onset dates correspond with greater annual snow-height increase at QIC.

Temporal offset between the surface snow δ^{18}O maximum and satellite-observed water vapor δD maximum indicates that the elevated surface snow δ^{18}O values are a product of postdepositional sublimation alteration. Snow δ^{18}O values during austral summer are in response to regional-scale atmospheric forcing, while postdepositional alteration of surface snow during austral winter is a product of in situ local forcing such as temperature, heating related to topography, or wind regimes on the ice-cap surface itself.

High-amplitude snow-height gain at QIC corresponds with precipitation maxima and OLR minima over the central and western Amazon Basin. Conversely, high-amplitude snow-height loss at QIC corresponds with precipitation maxima and OLR minima over the central Amazon Basin and northeastern Brazil.

Most of the snow-height gain at Quelccaya (~70% of the height gain is from the positive 90th and 60–90th percentile bins combined) is triggered by cold air incursions. This is snowfall from convection along cold fronts on the equatorward edge of near-surface low-MSE air that is advected from southern South America, east of the Andes, into the southwestern Amazon Basin. The cold air incursions, snow-height gain, and intense convection over the QIC have here been linked to increased midtroposphere humidity and decreased water vapor δD values, consistent with the amount effect.

4. Discussion

Near-surface (0 to 3 m) snow density values for 2003–2014 (448 kg m^{-3}) are consistent with previous values (400–500 kg m^{-3}) for the summit of Quelccaya [*Thompson*, 1980]. Average net annual increase, ~1.8 m snow height from 2003 to 2014, has decreased from about 2.1 m in previous decades [*Thompson et al.*, 1979; *Thompson*, 1980]. However, the standard deviation (0.3 m) for 2003–2014 places the previous mean value at about one standard deviation from the 2003–2014 mean. Water equivalent accumulation (~0.85 m water equivalent per year 2003–2014) has also decreased from about 1.3 m water equivalent during the 1980s and 1990s [*Thompson et al.*, 2011]. This is a notable decrease (~28%) in annual water equivalent accumulation at the summit of the QIC (2003–2014 compared with 1970s through 1990s). These reductions in snow accumulation at the summit of QIC may only in part be attributed to the 5% discrepancy between snowpit and AWS measurements of annual accumulation.

There is a 20‰ range of snow δ^{18}O values from the annual surface layers at the summit (2003–2014; −29.2‰ to −9.2‰) that is consistent with previously reported intraseasonal variability of ~22‰ [*Thompson*, 1980; *Thompson et al.*, 1993, 2011]. The mean δ^{18}O value (−18.8‰; σ = 4.1‰) for 2003–2014 is about 2‰ higher than the mean values reported for the 1970s, −21‰ [*Thompson and Dansgaard*, 1975; *Thompson et al.*, 1979], and about 2‰ less than the value of ~−17‰ for the 1991 summit core's surface layer [*Thompson et al.*, 1993]. As with the annual snow-height change, values from the 1970s and 1991 are within one standard deviation of the distribution of values from 2003 to 2014. Comparison of the mean δ^{18}O values, for the period of overlap (1969–1976) retrieved by both the 1976 (−19.4‰) and the 1991 (−17.4‰) summit core, indicates that alteration by meltwater percolation increased the mean value by 2‰.

The decreased snow water equivalent accumulation, combined with the recent alteration of snow δ^{18}O values at the summit of the QIC, caution (1) that there has possibly been a transition of the processes governing snowfall and accumulation, as well as snow δ^{18}O, at Quelccaya from the latter part of the twentieth century to today, and (2) continued monitoring of the QIC is necessary for a thorough comprehension of the ice cap's response to a rapidly changing climate.

Ice core $\delta^{18}O$ from QIC likely records wet season snowfall only and should be characterized by a gradual reduction of oxygen isotope values through the wet season as a function of continental recycling throughout the SASM season. At the top of the annual layers, oxygen isotope values increase not in accord with the seasonality of atmospheric water vapor stable isotopologue ratios but rather as a function of postdepositional alteration during the winter season. $\delta^{18}O$ ratios from snow layer tops may thus be linked to dry-season dynamics and atmosphere-snow exchange such as occurs in the firn's upper convective or diffusive zones [*Whillans and Grootes*, 1985; *Stichler et al*., 2001; *Huber et al*., 2006] as recently recognized at Greenland [*Steen-Larsen et al*., 2014]. Large hoar frost crystals suggestive of vapor transport and recrystallization have been observed at the summit of Quelccaya. Greenland surface snow $\delta^{18}O$ covaries, via isotopic exchange, with near-surface vapor $\delta^{18}O$ [*Steen-Larsen et al*., 2014]. Unlike Greenland, Quelccaya seasonal snow $\delta^{18}O$ and water vapor δD cycles are inversely correlated with temperature: stable isotope ratios are lowest during austral summer [*Thompson*, 1980; *Steen-Larsen et al*., 2013; *Ortega et al*., 2014].

5. Concluding Remarks

At QIC, annual snow-height increase is positively correlated with the duration of the snow accumulation season, particularly as a function of onset date. Monsoon onset date and duration are important not only for precipitation [*Lau and Yang*, 1996; *Gadgil*, 2003; *Li and Fu*, 2004], but they are tied to the large-scale dynamics [*Prive and Plumb*, 2007b; *Bordoni and Schneider*, 2010] and forcing from extratropical eddies [*Prive and Plumb*, 2007a; *Bordoni and Schneider*, 2008]. Extratropical cold air incursions during austral spring influence the initiation of the SASM wet season [*Li and Fu*, 2006]. Variable ventilation of monsoons by midlatitude low-MSE air has been shown to control the poleward extent of the monsoon domain by influencing near-surface MSE over the continent [*Prive and Plumb*, 2007a]. We expect that cold air incursion activity during the SASM season is diagnostic of monsoon intensity. Anomalously wet SASM years correspond with reduced SALLJ intensity at 700 hPa, suggestive of a positive correlation between cold air incursion activity and SASM precipitation [*Garreaud and Wallace*, 1998; *Hurley and Boos*, 2013]. Net snow-height increase at QIC during the period of this study is over 18 m (2003 to 2014), and cold air incursions, during DJF alone, account for more than 13 m (positive 90th and 60–90th percentiles combined). Because we have here tied the majority of snowfall at Quelccaya to cold air incursions, some of the variance in the ice record from the QIC likely records the paleoclimatic history of ventilation and intensity of the SASM. *Yin et al*. [2013] evaluated Coupled Model Intercomparison Project 5 model historical simulations of tropical South American precipitation. They found that anomalous upper troposphere westerlies during the transitional SON season lead to a dry precipitation bias by weakening the effect of cold air incursions. More recently, *Yin et al*. [2014] found that cold air incursions penetrating into the Amazon Basin are inhibited by poleward displacement of the Southern Hemisphere subtropical jet. Based on satellite observations of temperature in the lower stratosphere, *Fu and Lin* [2011] document a 0.6° poleward shift of the Southern Hemisphere subtropical jet since 1979. Cold air incursion activity over South America has been shown here to account for most of the snowfall at Quelccaya, and we expect that the behavior of these incursions on longer time scales are important for both sustaining the ice cap and deciphering the QIC's history as it regards the SASM. It is interesting to consider whether cold air incursion activity may be related to longer-period variability of snow $\delta^{18}O$ at Quelccaya. Snow $\delta^{18}O$ may reflect atmospheric vapor stable isotope ratios and variability as a function of changes in condensation temperature, cloud heights, amounts effects, or convective processes associated with cold air incursions [*Risi et al*., 2008; *Scholl et al*., 2009].

A 21 m core was recently (October 2014) extracted at the summit of the QIC, encompassing the continuous snow-height change history of the past decade. We expect that the continuous stable isotopologue values measured in this core will yield insight into how monsoon dynamics and intensity are related to snow $\delta^{18}O$ at Quelccaya. The processes identified here as relevant to snowfall at Quelccaya will be folded into the development of a process-based forward model that utilizes proxy data and observations at Quelccaya to reconstruct the paleoclimate of the SASM.

Acknowledgments

ERA-Interim reanalysis was obtained from the Research Data Archive (RDA) that is maintained by the Computational and Information Systems Laboratory at the National Center for Atmospheric Research (NCAR). NCAR is sponsored by the National Science Foundation (NSF). The original data are available from the RDA (http://rda.ucar.edu) in data set number ds627.0. GPCP 1° daily precipitation data were obtained from the NASA Goddard Space Flight Center (http://precip.gsfc.nasa.gov). NOAA OLR daily data were obtained from the Earth System Research Laboratory at (http://www.esrl.noaa.gov/psd/data/gridded/data.interp_OLR.html). TES Lite Products data were obtained from the NASA Jet Propulsion Laboratory (tes.jpl.nasa.gov/data/). The authors thank Camille Risi and Christian Frankenberg for GOSAT data. The authors gratefully acknowledge the insightful comments from two anonymous reviewers and the financial support from NSF-P2C2 (AGS-1303828), NSF Paleoclimate (9909201 and 0402557), and the NOAA Global Climate Observing System. Data unique to this study may be obtained upon request from the authors.

References

Apaestegui, J., et al. (2014), Hydroclimate variability of the northwestern Amazon Basin near the Andean foothills of Peru related to the South American monsoon system during the last 1600 years, *Clim. Past*, *10*, 1967–1981.

Arakawa, A., and W. Schubert (1974), Interaction of a cumulus cloud ensemble with the large-scale environment, Part I, *J. Atmos. Sci.*, *31*, 674–701.

Bird, B. W., M. B. Abbott, M. Vuille, D. T. Rodbell, N. D. Stansell, and M. F. Rosenmeier (2011), A 2,300-year-long annually resolved record of the South American summer monsoon from the Peruvian Andes, *Proc. Natl. Acad. Sci. U.S.A.*, *108*(2), 8583–8588.

Boers, N., A. Rheinwalt, B. Bookhagen, H. M. J. Barbosa, N. Marwan, J. Marengo, and J. Kurths (2014), The South American rainfall dipole: A complex network analysis of extreme events, *Geophys. Res. Lett.*, *41*, 7397–7405, doi:10.1002/2014GL061829.

Bordoni, S., and T. Schneider (2008), Monsoons as eddy-mediated regime transitions of the tropical overturning circulation, *Nat. Geosci.*, *1*, 515–519.

Bordoni, S., and T. Schneider (2010), Regime transitions of steady and time-dependent Hadley circulations: Comparison of axisymmetric and eddy-permitting simulations, *J. Atmos. Sci.*, *67*, 1643–1654.

Bradley, R. S. (2015), *Paleoclimatology: Reconstructing Climates of the Quaternary*, 3rd ed., pp., Elsevier, Oxford, U. K.

Bradley, R. S., M. Vuille, D. R. Hardy, and L. G. Thompson (2003), Low latitude ice cores record Pacific sea surface temperatures, *Geophys. Res. Lett.*, *40*(4), 1174, doi:10.1029/2002GL016546.

Bradley, R. S., F. Keimig, H. F. Diaz, and D. R. Hardy (2009), Recent changes in freezing level heights in the tropics with implications for the deglacierization of high mountain regions, *Geophys. Res. Lett.*, *36*, L17701, doi:10.1029/2009GL037712.

Brown, D., J. Worden, and D. Noone (2008), Comparison of atmospheric hydrology over convective continental regions using water vapor isotope measurements from space, *J. Geophys. Res.*, *113*, D15124, doi:10.1029/2007JD009676.

Brown, D., J. Worden, and D. Noone (2013), Characteristics of tropical and subtropical atmospheric moistening derived from Lagrangian mass balance constrained by measurements of HDO and H_2O, *J. Geophys. Res. Atmos.*, *118*, 54–72, doi:10.1029/2012JD018507.

Carvalho, L. M. V., C. Jones, and B. Liebmann (2004), The South Atlantic Convergence Zone: Intensity, form, persistence, and relationships with intraseasonal to interannual activity and extreme rainfall, *J. Clim.*, *17*, 88–108.

Chen, T.-C., S.-P. Weng, and S. Schubert (1999), Maintenance of austral summertime upper-tropospheric circulation over tropical South America: The Bolivian High-Nordeste Low system, *J. Atmos. Sci.*, *56*, 2081–2100.

Chou, C., and J. D. Neelin (2001), Mechanisms limiting the southward extent of the South American summer monsoon, *Geophys. Res. Lett.*, *28*, 2433–2436, doi:10.1029/2000GL012138.

Chou, C., and J. D. Neelin (2003), Mechanisms limiting the northward extent of the northern summer monsoons over North America, Asia, and Africa, *J. Clim.*, *16*, 406–425.

Chou, C., J. D. Neelin, and H. Su (2001), Ocean–atmosphere-land feedbacks in an idealized monsoon, *Q. J. R. Meteorol. Soc.*, *127*, 1869–1891.

Cohen, J. C. P., M. A. F. Silva Dias, and C. A. Nobre (1995), Environmental conditions associated with Amazonian squall lines: A case study, *Mon. Weather Rev.*, *123*, 3163–3174.

Cook, K. H., J.-S. Hsieh, and S. M. Hagos (2004), The Africa-South America intercontinental teleconnection, *J. Clim.*, *17*, 2851–2865.

Davis, M. E., L. G. Thompson, E. Mosley-Thompson, P.-N. Lin, V. N. Mikhalenko, and J. Dai (1995), Recent ice-core climate records from the Cordillera Blanca, Peru, *Ann. Glaciol.*, *21*, 225–230.

Dee, D. P., et al. (2011), Ther ERA-Interim reanalysis: Configuration and performance of the data assimilation system, *Q. J. R. Meteorol. Soc.*, *137*, 553–597.

Emanuel, K. A. (1995), On thermally direct circulations in moist atmospheres, *J. Atmos. Sci.*, *52*, 1529–1536.

Espinoza, J. C., J. Ronchail, M. Lengaigne, N. Quispe, Y. Silva, M. L. Bettolli, G. Avalos, and A. Llacza (2013), Revisiting wintertime cold air intrusions at the east of the Andes: Propogating features from subtropical Argentina to Peruvian Amazon and relationship with large-scale circulation patterns, *Clim. Dyn.*, *41*, 1983–2002.

Frankenberg, C., D. Wunch, G. Toon, C. Risi, R. Scheepmaker, J.-E. Lee, P. Wennberg, and J. Worden (2013), Water vapor isotoplogue retrievals from high-resolution GOSAT shortwave infrared spectra, *Atmos. Meas. Tech.*, *6*, 263–274.

Fu, Q., and P. Lin (2011), Poleward shift of subtropical jets inferred from satellite-observed lower-stratosphere temperatures, *J. Clim.*, *24*, 5597–5603.

Gadgil, S. (2003), The Indian monsoon and its variability, *Annu. Rev. Earth Planet. Sci.*, *31*, 429–467.

Galewsky, J. (2015), Constraining supersaturation and transport processes in a South American Cold-Air Outbreak using stable isotopologues of water vapor, *J. Atmos. Sci.*, *72*, 2055–2069.

Galewsky, J., and K. Samuels-Crow (2014), Water vapor isotopic composition of a stratospheric air intrusion: Measurements from the Chajnantor Plateau, Chile, *J. Geophys. Res. Atmos.*, *119*, 9679–9691, doi:10.1002/2014JD022047.

Gao, J., V. Masson-Delmotte, C. Risi, Y. He, and T. Yao (2013), What controls precipitation d18O in the southern Tibetan Plateau at seasonal and intra-seasonal scales? A case study at Lhasa and Nyalam, *Tellus B*, *65*, doi:10.3402/tellusb.v65i0.21043.

Garreaud, R., and J. M. Wallace (1998), Summertime incursions of midlatitude air into subtropical and tropical South America, *Mon. Weather Rev.*, *126*, 2713–2733.

Garreaud, R., M. Vuille, and A. C. Clement (2003), The climate of the Altiplano: Observed current conditions and mechanisms of past changes, *Palaeogeogr. Palaeoclimatol. Palaeoecol.*, *194*, 5–22.

Garreaud, R. D. (1999), Cold air incursions over subtropical and tropical South America: A numerical case study, *Mon. Weather Rev.*, *127*, 2823–2852.

Garreaud, R. D. (2000), Cold air incursions over subtropical South America: Mean structures and dynamics, *Mon. Weather Rev.*, *128*, 2544–2559.

Gat, J. R. (1996), Oxygen and hydrogen isotopes in the hydrologic cycle, *Annu. Rev. Earth Planet. Sci.*, *24*, 225–262.

Ginot, P., C. Kull, M. Schwikowski, U. Schotterer, and H. W. Gaggeler (2001), Effects of postdepositional processes on snow composition of a subtropical glacier (Cerro Tapado, Chilean Andes), *J. Geophys. Res.*, *106*, 32,375–32,386, doi:10.1029/2000JD000071.

Ginot, P., C. Kull, U. Schotterer, M. Schwikowski, and H. W. Gaggeler (2006), Glacier mass balance reconstruction by sublimation induced enrichment of chemical species on Cerro Tapado [Chilean Andes], *Clim. Past*, *2*, 21–30.

Hamazaki, T., Y. Kaneko, A. Kuze, and K. Kondo (2005), Fourier transform spectrometer for Greenhouse Gases Observing Satellite (GOSAT), in *Proceedings SPIE Enabling Sensor and Platform Technologies for Spaceborne Remote Sensing*, vol. 5659, 73 pp., SPIE—The International Society for Optical Engineering Bellingham, Wash., doi:10.1117/12.581198.

Hardy, D. R., M. Vuille, and R. S. Bradley (2003), Variability of snow accumulation and isotopic composition on Nevado Sajama, Bolivia, *J. Geophys. Res.*, *108*(D22), 4693, doi:10.1029/2003JD003623.

He, Y., et al. (2015), Impact of atmospheric convection on south Tibet summer precipitation isotopologue composition using a combination of in situ measurements, satellite data and atmospheric general circulation modeling, *J. Geophys. Res. Atmos.*, *120*, 3852–3871, doi:10.1002/2014JD022180.

Hoffman, G., et al. (2003), Coherent isotope history of Andean ice cores over the last century, *Geophys. Res. Lett.*, *30*(4), 1179, doi:10.1029/2002GL014870.

Huber, C., M. Leuenberger, R. Spahni, J. Fluckiger, J. Schwander, T. F. Stocker, S. Johnsen, A. Landais, and J. Jouzel (2006), Isotope calibrated Greenland temperature record over marine isotope stage 3 and its relation to CH_4, *Earth Planet. Sci. Lett.*, *243*, 504–519.

Huffman, G. J., R. F. Adler, M. Morrisey, D. T. Bolvin, S. Curtis, R. Joyce, B. McGavock, and J. Susskind (2001), Global precipitation at one-degree daily resolution from multi-satellite observations, *J. Hydrometeorol.*, *2*, 36–50.

Huffman, G. J., R. F. Adler, D. T. Bolvin, G. Gu, E. J. Nelkin, K. P. Bowman, Y. Hong, E. F. Stocker, and D. B. Wolff (2007), The TRMM Multisatellite Precipitation Analysis (TMPA): Quasi-global, multiyear, combined-sensor precipitation estimates at fine scales, *J. Hydrometeorol.*, *8*, 38–55.

Hurley, J. V., and W. R. Boos (2013), Interannual variability of monsoon precipitation and local subcloud equivalent potential temperature, *J. Clim.*, *26*, 9507–9527.

IAEA/WMO (2015), Global Network of Isotopes in Precipitation, The GNIP Database. [Available at http://www.iaea.org/water.]

Kanner, L. C., S. J. Burns, H. Cheng, R. Lawrence Edwards, and M. Vuille (2013), High-resolution variability of the South American summer monsoon over the last seven millenia: Insights from a speleothem record from the central Peruvian Andes, *Quat. Sci. Rev.*, *75*, 1–10.

Kodama, Y. (1992), Large-scale common features of subtropical precipitation zones (the Baiu Frontal Zone, the SPCZ, and the SACZ), Part I: Characteristics of subtropical frontal zones, *J. Meteorol. Soc. Jpn.*, *70*, 813–836.

Kummerow, C., W. Barnes, and T. Kozu (1998), The Tropical Rainfall Measuring Mission (TRMM) sensor package, *J. Atmos. Oceanic Technol.*, *15*, 809–817.

Kummerow, C., et al. (2000), The status of the Tropical Rainfall Measuring Mission (TRMM) after two years in orbit, *J. Appl. Meteorol. Climatol.*, *39*, 1965–1982.

Kuze, A., H. Suto, M. Nakajima, and T. Hamazaki (2009), Thermal and near infrared sensor for carbon observation Fourier-transform spectrometer on the Greenhouse Gases Observing Satellite for greenhouse gases monitoring, *Appl. Opt.*, *48*, 6716–6733.

Lau, K.-M., and S. Yang (1996), Seasonal variation, abrupt transition, and intraseasonal variability associated with the Asian summer monsoon in the GLA GCM, *J. Clim.*, *9*, 965–985.

Lee, J., C. Risi, I. Fung, J. Worden, R. A. Scheepmaker, B. Lintner, and C. Frankenberg (2012), Asian monsoon hydrometeorology from TES and SCIAMACHY water vapor isotope measurements and LMDZ simulations: Implications for speleothem climate record interpretation, *J. Geophys. Res.*, *117*, D15112, doi:10.1029/2011JD017133.

Lenters, J. D., and K. H. Cook (1997), On the origin of the Bolivian High and related circulation features of the South American climate, *J. Atmos. Sci.*, *54*, 656–677.

Li, W., and R. Fu (2004), Transition of the large-scale atmospheric and land surface conditions from the dry to the wet season over Amazonia as diagnosed by the ECMWF Re-Analysis, *J. Clim.*, *17*, 2637–2651.

Li, W., and R. Fu (2006), Influence of cold air intrusions on the wet season onset over Amazonia, *J. Clim.*, *19*, 257–275.

Liebmann, B., and C. A. Smith (1996), Description of a complete (interpolated) outgoing longwave radiation dataset, *Bull. Am. Meteorol. Soc.*, *77*, 1275–1277.

Marengo, J. A., M. W. Douglas, and P. L. Silva Dias (2002), The South American low-level jet east of the Andes during the 1999 LBA-TRMM and LBA-WET AMC campaign, *J. Geophys. Res.*, *107*(D20), 8079, doi:10.1029/2001JD001188.

NASA (2014), Jet Propulsion Laboratory, Aura TES Group, TES Lite Products. [Available at http://avdc.gsfc.nasa.gov.]

Nie, J., W. R. Boos, and Z. Kuang (2010), Observational evaluation of a convective quasi-equilibrium view of monsoons, *J. Clim.*, *23*, 4416–4428.

Nogues-Paegle, J., and K. C. Mo (1997), Alternating wet and dry conditions over South America during summer, *Mon. Weather Rev.*, *125*, 279–291.

Noone, D. (2012), Pairing measurements of the water vapor isotope ratio with humidity to deduce atmospheric moistening and dehydration in the tropical midtroposphere, *J. Clim.*, *25*, 4476–4494.

Ortega, P., D. Swingedouw, V. Masson-Delmotte, C. Risi, B. Vinther, P. Yiou, R. Vautard, and K. Yoshimura (2014), Characterizing atmospheric circulation signals in Greenland ice cores: Insights from a weather regime approach, *Clim. Dyn.*, *43*, 2585–2605.

Prive, N. C., and R. A. Plumb (2007a), Monsoon dynamics with interactive forcing. Part II: Impact of eddies and asymmetric geometries, *J. Atmos. Sci.*, *64*, 1431–1442.

Prive, N. C., and R. A. Plumb (2007b), Monsoon dynamics with interactive forcing. Part I: Axisymmetric studies, *J. Atmos. Sci.*, *64*, 1417–1430.

Rabatel, A., et al. (2013), Current state of glaciers in the tropical Andes: A multi-century perspective on glacier evolution and climate change, *Cryosphere*, *7*, 81–102.

Ramage, C. S. (1971), *Monsoon Meteorology*, 269 pp., Academic Press, New York.

Rickenbach, T. M., R. N. Ferreira, J. B. Halverson, D. L. Herdeis, and M. A. F. Silva Dias (2002), Modulation of convection in the southwestern Amazon Basin by extratropical stationary fronts, *J. Geophys. Res.*, *107*(D20), 8040, doi:10.1029/2000JD000263.

Risi, C., S. Bony, and F. Vimeux (2008), Influence of convective processes on the isotopic composition (δ^{18}O and δD) of precipitation and water vapor in the tropics: 2. Physical interpretation of the amount effect, *J. Geophys. Res.*, *113*, D19306, doi:10.1029/2008JD009943.

Risi, C., et al. (2012), Process-evaluation of tropospheric humidity simulated by general circulation models using water vapor isotopic observations: 2. Using isotopic diagnostics to understand the mid and upper tropospheric moist bias in the tropics and subtropics, *J. Geophys. Res.*, *117*, D05304, doi:10.1029/2011JD016623.

Risi, C., D. Noone, C. Frankenberg, and J. Worden (2013), Role of continental recycling in intraseasonal variations of continental moisture as deduced from model simulations and water vapor isotopic measurements, *Water Resour. Res.*, *49*, 4136–4156, doi:10.1002/wrcr.20312.

Romatschke, U., and R. A. Houze (2013), Characteristics of precipitating convective systems accounting for the summer rainfall of tropical and subtropical South America, *J. Hydrometeorol.*, *14*, 25–46.

Samuels-Crow, K., J. Galewsky, D. R. Hardy, Z. D. Sharp, J. Worden, and C. Braun (2014), Upwind convective influences on the isotopic composition of atmospheric water vapor over the tropical Andes, *J. Geophys. Res. Atmos.*, *119*, 7051–7063, doi:10.1002/2014JD021487.

Scholl, M. A., J. B. Shanley, J. P. Zegarra, and T. B. Coplen (2009), The stable isotope amount effect: New insights from NEXRAD echo tops, Luquillo Mountains, Puerto Rico, *Water Resour. Res.*, *45*, W12407, doi:10.1029/2008WR007515.

Silva Dias, M. A. F., et al. (2002), Cloud and rain processes in a biosphere-atmosphere interaction context in the Amazon Basin, *J. Geophys. Res.*, *107*(D20), 8072, doi:10.1029/2001JD000335.

Siqueira, J. R., and L. A. Toledo-Machado (2004), Influence of the frontal systems on the day-to-day convection variability over South America, *J. Clim.*, *17*, 1754–1766.

Siqueira, J. R., W. B. Rossow, L. A. Toledo-Machado, and C. Pearl (2005), Structural characteristics of convective systems over South America related to cold-frontal incursions, *Mon. Weather Rev.*, *133*, 1045–1064.

Steen-Larsen, H. C., et al. (2013), Continuous monitoring of summer surface water vapor isotopic composition above the Greenland Ice Sheet, *Atmos. Chem. Phys.*, *13*, 4815–4828.

Steen-Larsen, H. C., et al. (2014), What controls the isotopic composition of Greenland surface snow?, *Clim Past*, *10*, 377–392.

Stichler, W., U. Schotterer, K. Frohlich, P. Ginot, C. Kull, H. W. Gaggeler, and B. Pouyaud (2001), Influence of sublimation on stable isotope records recovered from high-altitude glaciers in the tropical Andes, *J. Geophys. Res.*, *106*, 22,613–22,620, doi:10.1029/2001JD900179.

Thompson, L. G. (1980), Glaciological investigations of the tropical Quelccaya Ice Cap, Peru, *J. Glaciol.*, *25*(91), 69–84.

Thompson, L. G., and W. Dansgaard (1975), Oxygen isotope and microparticle studies of snow samples from Quelccaya Ice Cap, Peru, *Antarct. J. U. S.*, *10*(1), 24–26.
Thompson, L. G., S. Hastenrath, and B. M. Arnao (1979), Climatic ice core records from the tropical Quelccaya Ice Cap, *Science*, *203*, 1240–1243.
Thompson, L. G., E. Mosley-Thompson, J. F. Bolzan, and B. R. Koci (1985), A 1500-year record of tropical precipitation in ice cores from the Quelccaya Ice Cap, Peru, *Science*, *229*(4717), 971–973.
Thompson, L. G., E. Mosley-Thompson, W. Dansgaard, and P. M. Grootes (1986), The little ice age as recorded in the stratigraphy of the tropical Quelccaya Ice Cap, *Science*, *234*, 361–364.
Thompson, L. G., E. Mosley-Thompson, M. Davis, P. N. Lin, T. Yao, M. Dyurgerov, and J. Dai (1993), "Recent warming": Ice core evidence from tropical ice cores with emphasis on central Asia, *Global Planet. Change*, *7*, 145–156.
Thompson, L. G., E. Mosley-Thompson, H. Brecher, M. Davis, B. Leon, D. Les, P.-N. Lin, T. Mashiotta, and K. Mountain (2006), Abrupt tropical climate change: Past and present, *Proc. Natl. Acad. Sci. U.S.A.*, *103*, 10,536–10,543.
Thompson, L. G., E. Mosley-Thompson, M. Davis, and H. Brecher (2011), Tropical glaciers, recorders and indicators of climate change, are disappearing globally, *Ann. Glaciol.*, *52*(59), 23–34.
Thompson, L. G., E. Mosley-Thompson, M. E. Davis, V. S. Zagorodnov, I. M. Howat, V. N. Mikhalenko, and P.-N. Lin (2013), Annually resolved ice core records of tropical climate variability over the past ~1800 years, *Science*, *340*, 945–950.
Vera, C. S., and P. K. Vigliarolo (2000), A diagnostic study of cold-air outbreaks over South America, *Mon. Weather Rev.*, *128*, 3–24.
Vera, C. S., et al. (2006), Toward a unified view of the American monsoon systems, *J. Clim.*, *19*, 4977–5000.
Vimeux, F., R. Gallaire, S. Bony, G. Hoffman, and C. H. Chiang (2005), What are the climate controls on D in precipitation in the Zongo Valley (Bolivia)? Implications for the Illimani ice core interpretation, *Earth Planet. Sci. Lett.*, *240*, 205–220.
Vimeux, F., P. Ginot, M. Schwikowski, M. Vuille, G. Hoffman, L. G. Thompson, and U. Schotterer (2009), Climate variability during the last 1000 years inferred from Andean ice cores: A review of methodology and recent results, *Palaeogeogr. Palaeoclimatol. Palaeoecol.*, *281*, 229–241.
Vuille, M., and F. Keimig (2004), Interannual variability of summertime convective cloudiness and precipitation in the central Andes derived from ISCCP-B3 data, *J. Clim.*, *17*, 3334–3348.
Vuille, M., and M. Werner (2005), Stable isotopes in precipitation recording South American summer monsoon and ENSO variability: Observations and model results, *Clim. Dyn.*, *25*, 401–413.
Vuille, M., D. R. Hardy, C. Braun, F. Keimig, and R. S. Bradley (1998), Atmospheric circulation anomalies associated with 1996/1997 summer precipitation events on Sajama Ice Cap, Bolivia, *J. Geophys. Res.*, *103*, 11,191–11,204, doi:10.1029/98JD00681.
Vuille, M., R. S. Bradley, and F. Keimig (2000), Interannual climate variability in the central Andes and its relation to tropical Pacific and Atlantic forcing, *J. Geophys. Res.*, *105*, 12,447–12,460, doi:10.1029/2000JD900134.
Vuille, M., R. S. Bradley, M. Werner, R. Healy, and F. Keimig (2003), Modeling δ^{18}O in precipitationover the tropical Americas: 1 Interannual variability and climatic controls, *J. Geophys. Res.*, *108*(D6), 4174, doi:10.1029/2001JD002038.
Vuille, M., B. Francou, P. Wagnon, I. Juen, G. Kaser, B. G. Mark, and R. S. Bradley (2008), Climate change and tropical Andean glaciers: Past, present, and future, *Earth Sci. Rev.*, *89*(3–4), 79–96.
Vuille, M., S. J. Burns, B. L. Taylor, F. W. Cruz, B. W. Bird, M. B. Abbott, L. C. Kanner, H. Cheng, and V. F. Novello (2012), A review of the South American monsoon history as recorded in stable isotopic proxies over the past two millenia, *Clim. Past*, *8*, 1309–1321.
Whillans, I. M., and P. M. Grootes (1985), Isotopic diffusion in cold snow and firn, *J. Geophys. Res.*, *90*, 3910–3918, doi:10.1029/JD090iD02p03910.
Winkler, M., I. Juen, T. Molg, P. Wagnon, J. Gomez, and G. Kaser (2009), Measured and modeled sublimation on the tropical Glaciar Artesonraju, Peru, *Cryosphere*, *3*, 21–30.
Worden, J., et al. (2006), Tropospheric Emission Spectrometer observations of the tropospheric HDO/H_2O ratio: Estimation approach and characterization, *J. Geophys. Res.*, *111*, D16309, doi:10.1029/2005JD006606.
Worden, J., et al. (2007), Importance of rain evaporation and continental convection in the tropical water cycle, *Nature*, *445*, 528–532.
Worden, J., D. Noone, J. Galewsky, A. Bailey, K. Bowman, D. Brown, J. V. Hurley, S. Kulawik, J. Lee, and M. Strong (2011), Estimate of bian in Aura TES HDO/H2O profiles from comparison of TES and in situ HDO/H2O measurements at the Mauna Loa Observatory, *Atmos. Chem. Phys.*, *11*, 4491–4503.
Worden, J., S. Kulawik, C. Frankenberg, V. Payne, K. Bowman, K. Cady-Peirara, K. Wecht, and J.-E. Lee (2012), Profiles of CH_4, HDO, H_2O, and N_2O with improved lower tropospheric vertical resolution from Aura TES radiances, *Atmos. Meas. Tech.*, *5*, 397–411.
Yin, L., R. Fu, E. Shevliakova, and R. E. Dickinson (2013), How well can CMIP5 simulate precipitation and its controlling processes over tropical South America?, *Clim. Dyn.*, *41*, 3127–3143.
Yin, L., R. Fu, Y. Zhang, P. A. Arias, D. N. Fernando, W. Li, K. Fernandes, and A. R. Bowerman (2014), What controls the interannual variation of the wet season onsets over the Amazon?, *J. Geophys. Res. Atmos.*, *119*, 2314–2328.
Zhou, J., and K.-M. Lau (1998), Does a monsoon climate exist over South America?, *J. Clim.*, *11*, 1020–1040.